University of Birmingham Research at Birmingham

Synergistic deformation pathways in a TWIP steel at cryogenic temperatures

Tang, Lei; Wang, Li; Wang, Minshi; Liu, Huibin; Kabra, Saurabh; Chiu, Yulung; Cai, Biao

DOI:
10.1016/j.actamat.2020.09.075

License:
Creative Commons: Attribution-NonCommercial-NoDerivs (CC BY-NC-ND)

Document Version
Peer reviewed version

Citation for published version (Harvard):
Tang, L, Wang, L, Wang, M, Liu, H, Kabra, S, Chiu, Y & Cai, B 2020, 'Synergistic deformation pathways in a TWIP steel at cryogenic temperatures: in situ neutron diffraction', *Acta Materialia*, vol. 200, pp. 943-958.
https://doi.org/10.1016/j.actamat.2020.09.075

Link to publication on Research at Birmingham portal

General rights
Unless a licence is specified above, all rights (including copyright and moral rights) in this document are retained by the authors and/or the copyright holders. The express permission of the copyright holder must be obtained for any use of this material other than for purposes permitted by law.

•Users may freely distribute the URL that is used to identify this publication.
•Users may download and/or print one copy of the publication from the University of Birmingham research portal for the purpose of private study or non-commercial research.
•User may use extracts from the document in line with the concept of ‘fair dealing’ under the Copyright, Designs and Patents Act 1988 (?)
•Users may not further distribute the material nor use it for the purposes of commercial gain.

Where a licence is displayed above, please note the terms and conditions of the licence govern your use of this document.

When citing, please reference the published version.

Take down policy
While the University of Birmingham exercises care and attention in making items available there are rare occasions when an item has been uploaded in error or has been deemed to be commercially or otherwise sensitive.

If you believe that this is the case for this document, please contact UBIRA@lists.bham.ac.uk providing details and we will remove access to the work immediately and investigate.

Download date: 27. Apr. 2024

Synergistic deformation pathways in a TWIP steel at cryogenic temperatures: *in situ* neutron diffraction

Lei Tang[a], Li Wang[b, c], Minshi Wang[a], Huibin Liu[d], Saurabh Kabra[e], Yulung Chiu[a], Biao Cai[a*]

a School of Metallurgy and Materials, University of Birmingham, B15 2TT, United Kingdom
b State Key Laboratory of Powder Metallurgy, Central South University, Changsha, 410083, China
c Institute of Materials Research, Helmholtz-Zentrum Geesthacht, Max-Planck-Strasse 1, Geesthacht, D-21502, Germany
d BAOSHAN IRON & STEEL CO., LTD, Shanghai 201900, P.R. China
e ISIS Facility, Rutherford Appleton Laboratory, Didcot OX11 0QX, United Kingdom
* Corresponding author.
Email address: b.cai@bham.ac.uk

Abstract

High manganese steels are promising candidates for applications in cryogenic environments. In this study, we investigate the mechanical and microstructural responses of a high manganese twinning induced plasticity (TWIP) steel at a low-temperature range (from 373 to 77 K) via *in situ* neutron diffraction qualification and correlative microscopy characterization. During plastic deformation, stacking fault probability and dislocation density increased at a faster rate at a lower temperature, hence, higher dislocation density and denser mechanical twins were observed, confirmed by microscopic observation. Stacking fault energy was estimated, dropping linearly from 34.8 mJm^{-2} at 373 K to 17.2 mJm^{-2} at 77 K. A small amount of austenite transferred to martensite when deforming at 77 K. The contributions to flow stress from solutes, grain boundary, dislocation, and twinning were determined at different temperatures, which shows that the high work strain hardening capacity of the TWIP steel originates from the synergetic strengthening effects of dislocations and twin-twin networks. These findings reveal the relationship among stacking fault energy, microstructure, and deformation mechanisms at the low-temperature range, paving a way in designing TWIP steels with the superb mechanical performance for cryogenic applications.

Keywords:

Cryogenic temperatures; Deformation twinning; Neutron diffraction; deformation pathways.

1. Introduction

There is a rapidly growing demand for development of metallic materials to be used at cryogenic temperatures such as liquified gas (e.g. natural gas and hydrogen) storage and transportation, nuclear fusion devices, and for outer-space exploration [1–3]. High Mn austenite steels are promising candidates not only due to their superior ability to resist low-

temperature cracking, excellent work hardening capacity and the associated superb strength-ductility combination [2–5], but also because that their costs are lower compared to austenite stainless steels [6], 9% Ni steels [7] and medium/high entropy alloys [8,9].
High Mn austenite steels with Mn content in the range of 15 to 30 wt.% are known to trigger nano-twinning during deformation [2,10], achieving excellent mechanical performance with high strain hardening. The activation of twinning effects is closely related to the temperature- and composition-dependent stacking fault energy (SFE) [11–13]. When SFE is higher than 45 mJm^{-2}, dislocation sliding takes the main role, whereas twinning is favored when SFE dropping to the range of 18~45 mJm^{-2}. If the SFE is further decreased to a very low level (<18 mJm^{-2}), phase transformation can be triggered due to the negative value of molar Gibbs energy of the transition from FCC-austenite to HCP- or/and BCT-martensite. Although this relationship between SFE and deformation mechanisms is well known, the measurement of SFE in high Mn steels at the low-temperature regime has rarely been reported. Theoretical calculation based on thermodynamics [4] and first principle [14] was used to determine the temperature dependence of SFE, but experimental measurements are rare and critically needed for model validation.

Measurement of SFE of high Mn steels at cryogenic temperature is, hence, valuable for alloy development and understanding of deformation mechanisms. SFE can be obtained usually from transmission electron microscope (TEM) micrographs of unloaded specimens deformed to a certain strain [15,16]. This means that for cryogenic deformed specimens, we have to raise the temperature of the frozen samples to room temperature for sample preparation and TEM observation, which could lead to a significant change of the stacking fault structure hence the SFE measurement may not be reliable. Recently, *in situ* methods for mapping microstructure evolution during cryogenic deformation have been developed, such as *in situ* TEM [17] and *in situ* neutron diffraction [8,18,19]. *In situ* TEM shows remarkable advantages in observing the dislocation motion, slip band formation and primary/secondary twinning formation during deformation and should be a promising approach for SFE measurement, although implementation of *in situ* TEM at extremely low temperature is difficult [17,20]. *In situ* neutron diffraction combined with loading at cryogenic temperatures, on the other hand, not only can quantitatively depict the microstructural evolution of bulk materials (e.g., interplanar crystal lattice spacing [4], phase identification [21] and dislocation density [8,22]), but also allows us to measure SFE at extremely low temperatures as low as 15 K [19].

Although twinning is known to occur during the deformation of high Mn steels with SFE between 18 to 45 mJm^{-2}, the contribution of deformation-induced twins to their high work hardening capacity is under debate. It is widely accepted that during deformation, strain-induced twinning boundary serves as an effective barrier to impede dislocation gliding by reducing their mean-free-path. This leads to substantial strength enhancement under progressing strain, which is best known as “dynamic Hall-Petch effect” [23,24], providing sustained high work hardening rate. However, this concept was challenged recently. Liang et al. [25] demonstrated that dislocation motion is the main source for the high work hardening rate of TWIP steels while the twinning contribution is insignificant. Therefore, it is important to further shed light on the contributions of twinning and dislocation towards the work hardening.

Herein, we investigated the cooperative strengthening effects from dislocation motion and mechanical twinning in a high Mn TWIP steel (Fe-24Mn-4Cr-0.5C-0.5Cu) at a low-temperature range (from 373 to 77 K). The *in situ* neutron diffraction and tensile testing were performed to capture the microstructure evolution during deformation. The diffraction spectra were analyzed to obtain manifold microstructural parameters (e.g., lattice strain, stacking fault probability, SFE and dislocation density). After the tensile tests, microscopic observation has been carried out on the fractured samples to characterize the microstructure. Additionally, the strengthening contributions from various strengthening mechanisms have been determined at different deformation temperatures. This work provides an in-depth micro-mechanical understanding of the superior mechanical properties via dislocation-TWIP collective deformation mechanism.

2. Materials and methods

2.1 Material processing

The material was provided by Baosteel company. High purity metals (purity≥99.9%) were melted to cast an ingot with a composition of Fe-24Mn-4Cr-0.5Cu-0.5C (wt.%) by vacuum induction melting and casting. After homogenization at 1473 K for 48 h, the ingot was then subjected to hot rolling at 1200 K, followed by water quenching to room temperature.

2.2 *in situ* Neutron diffraction

In situ time-of-flight (TOF) neutron diffraction measurements during tensile tests were carried out on the ENGIN-X diffractometer with a stress rig, provided by ISIS spallation neutron source, the Rutherford Appleton Laboratory, UK [26]. The schematic illustration of the *in situ* TOF neutron diffraction experiment is shown in Fig. 1a. The incident beam, containing pulses of neutrons with a continuous range of speed and therefore wavelength, traveled through the moderator and was defined by slits with size of 4×4 mm^2. Two ±90° detector banks, radial and axial one, were mounted perpendicularly to the incident beam direction. They are capable of continuously collecting diffracted neutron beams from crystallographic grain planes subjected to compressing and tensile force, respectively. The intersection of the incident beam and 4 mm diffraction beam (defined by the width of collimator) determined the scattering gauge volume to be $4 \times 4 \times 4$ mm^3. Dog-bone tensile samples (Fig. 1c) with gauge volume of Φ 8×32 mm^3 were placed at a cryogenic chamber, which provides a high-vacuum environment ($<10^{-5}$ Pa) (Fig. 1b). Deformation temperature change was achieved by a built-in heater and two liquid helium tubes [27]. The temperature was stabilized for 30 minutes at the high vacuum state before tensile loading and collecting diffraction signals. The tensile forces were provided by an Instron stress rig with a load capability of ±100 kN mounted horizontally and 45° to the incident beam. A series of measurements were performed during the tensile tests and each diffraction pattern collection consumes 20 minutes between tensile loading steps, iterating until sample fracture. An extensometer was used to measure the strain during tensile loading. Prior to data collection, a standard sample (CeO_2) was used for precise calibration of the experimental geometry (e.g., primary and secondary flight path distance) and for subtraction of the instrumental broadening effect. The GSAS software package was applied to perform peak fitting (with pseudo-Voigt function) and Rietveld refinement, allowing the determination of peak position, full width at half maximum (FWHM) and lattice parameter. The lattice strain is defined as the change of inter-planar distance of a given grain family due to the applied stress. The inter-planar spacing from different crystallographic plane $\{hkl\}$ without stress (d_{hkl}^0) and under different stress conditions (d_{hkl}) were applied to evaluate the evolution of lattice strain (ε_{hkl}^{exp}) via:

$$\varepsilon_{hkl}^{exp} = \frac{d_{hkl} - d_{hkl}^0}{d_{hkl}^0} \tag{1}$$

To estimate the contribution of dislocation multiplication to the strength enhancement, the quantitatively analysis of dislocation density was necessary. We performed dislocation density calculation based on a modified Williamson-Hall method [28,29]. The detailed calculation procedure can be found in the Supplementary Material.

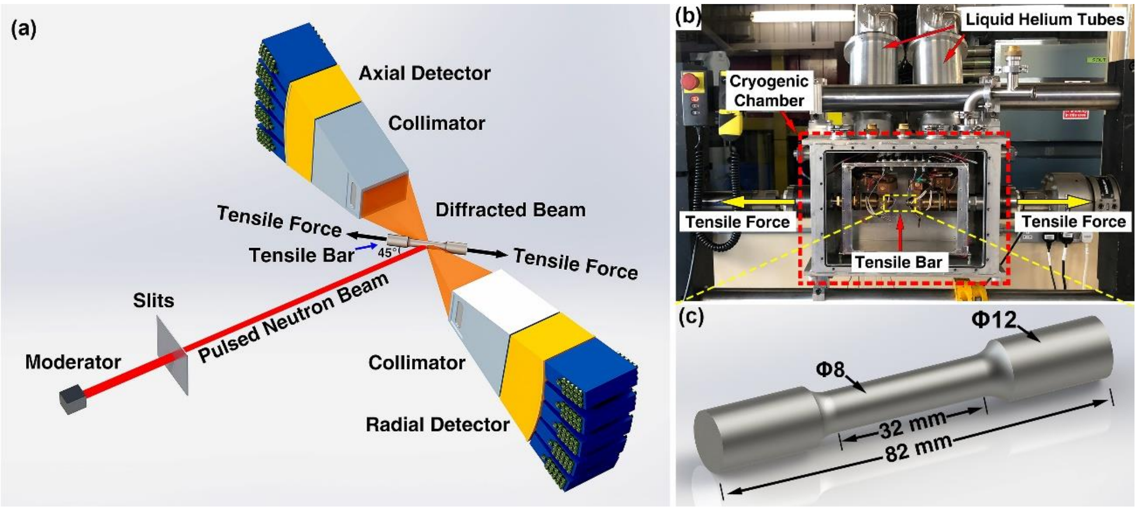

Fig. 1 (a) Schematic illustration of *in situ* neutron diffraction facility at ISIS, neutron and muon source; (b) the size of tensile bar; and (c) the cryo-chamber and hydraulic system.

2.3 Microstructure characterization

Samples for microstructure observation were sectioned from the fractured tensile bars after the tensile tests. After mechanical grinding and polishing, a solution consisting of dilute hydrochloric acid and iron chloride was used for etching before optical microscope (OM) observation. Electron backscatter diffraction (EBSD) was performed on a field emission gun scanning electron microscope (FEI Sirion 200) equipped with an HKL EBSD detector and Channel 5 software. The EBSD maps of the as-received material are shown as image quality maps and inverse pole figure (IPF) maps perpendicular to the rolling direction (RD). The RD was marked in EBSD maps. The scanning electron microscope (SEM) beam parameters were set to a voltage of 20 kV, current of 25 nA, spot size of 6.5, working distance of 168 mm and the scanning step size was set to 0.7 μm for the as-fabricated sample and to 0.03 μm for deformed samples. The EBSD data was then analyzed with a Matlab package, MTEX [30]. Misorientation angle less than 2° were ignored during the analysis to avoid ambiguous grain boundaries. For transmission electron microscope (TEM) and scanning transmission electron microscope (STEM) characterization, thin foils obtained by grinding and polishing were prepared by twin-jet electropolishing with a constant current of ~150 mA in a solution of 5 % perchloric acid and 95 % methanol cooled to -30 ℃. TEM and STEM characterization was then performed on a JOEL 2100 and FEI TITAN 30-800, respectively.

3. Results

3.1 Microstructure of the as-fabricated material

The typical IPF map in Fig. 2a shows the grain structure of the as-fabricated TWIP steel, which mainly consisted of large equiaxed grains with a small fraction of recrystallized grains. The average grain size was 14.0 ± 1.2 μm determined by performing line-intercept method on several optical micrographs, which is consistent with the EBSD results. Corresponding misorientation distribution was plotted in Fig. 2b, showing that its average grain misorientation angle was 28.3% with the fraction of low angle grain boundary (i.e. grain misorientation angle in the range of 2-15°) reaching a high level of 47.6%. Dislocation-tangling and dislocation-free zones were observed and shown in Fig. 2c and 2d, respectively. The dislocation networks, unevenly distributed, might be induced during the hot rolling and following quenching process.

3.2 Mechanical properties

Fig. 3a shows the engineering/true stress-strain curves of the alloy deformed at different temperatures. Corresponding mechanical properties (yielding strength (σ_{YS}), ultimate tensile strength (σ_{UTS}), total elongation and work hardening capacity (WHC)) were summarized with respect to deformation temperature in Fig. 3b. The WHC was calculated with the following equation [31]:

$$WHC = \frac{\sigma_{0.4} - \sigma_{YS}}{MG} \tag{2}$$

, where $\sigma_{0.4}$ is the true stress at a true strain of 0.4, G is the shear modulus and M=3.06 is the Taylor factor. At 373 K, the steel showed very large elongation of 0.68 and relatively low strength (σ_{YS} of 354 MPa and σ_{UTS} of 796 MPa). The σ_{YS} , σ_{UTS} and WHC increased almost linearly with the dropping of temperature (as shown in Fig. 3b and Table. (1)). An excellent combination of mechanical properties was achieved at 77 K, reaching σ_{YS} of 760 MPa, σ_{UTS} of 1312 MPa and total elongation of 0.56. The WHC increased from 3.46×10^{-3} at 373 K to 4.99×10^{-3} at 77 K. The alloy showed good ductility across the temperature range, with the total elongation remaining at a high level of ~0.55 or higher.

In order to further analyze the hardening behavior at different temperatures, the strain hardening rate (SHR, $d\sigma / d\varepsilon$) at different temperatures was plotted with respect to true stress in Fig. 3c. The SHR curves can be roughly divided into three stages (separated by dashed lines). At 373 K, the SHR curve kept dropping with the increase of true stress but the dropping speed varied among stages. At 293, 173 and 77 K, the SHR curves shared a very similar pattern: the SHR dropped rapidly at the first stage due to an elastic-plastic transition; Then they increased slightly at Stage II but dropped again at Stage III. The length of Stage II increased with decreasing temperature. At 293 K, Stage II ranged from 614 to 841 MPa and it was then expanded at 173 K (from 804 to 1200 MPa). While at 77 K Stage

II lasted from 1008 to 1700 MPa until almost approaching failure. Besides, as shown in Fig. 3c, the dropping of deformation temperature also pushed the elastic-plastic transition stress (from Stage I to Stage II) to higher stress levels (521 MPa at 373 K, 614 MPa at 293 K, 804 MPa at 173 K and 1008 MPa at 77 K). The Young's modulus (*E*) as shown in Table 2 was determined by the slope of the linear fitting function of the true stress/strain curve at the elastic stage. There are small variations of Young's modulus between different temperatures.

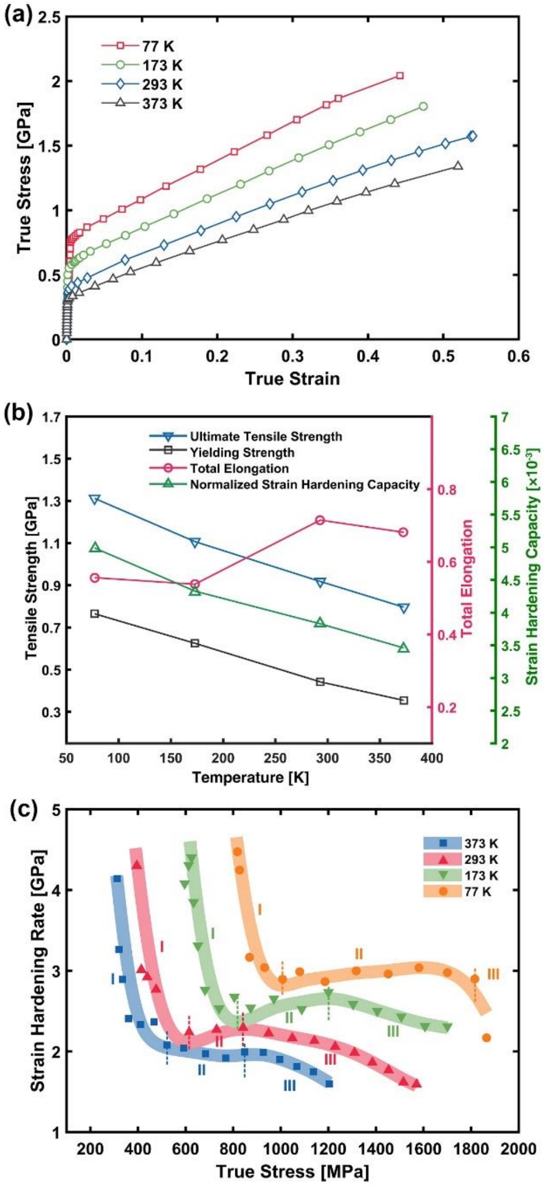

Fig. 3 Mechanical performance of the TWIP steel at different temperatures: (a) true stress-strain curves; (b) mechanical properties versus temperatures; and (c) strain hardening rate.

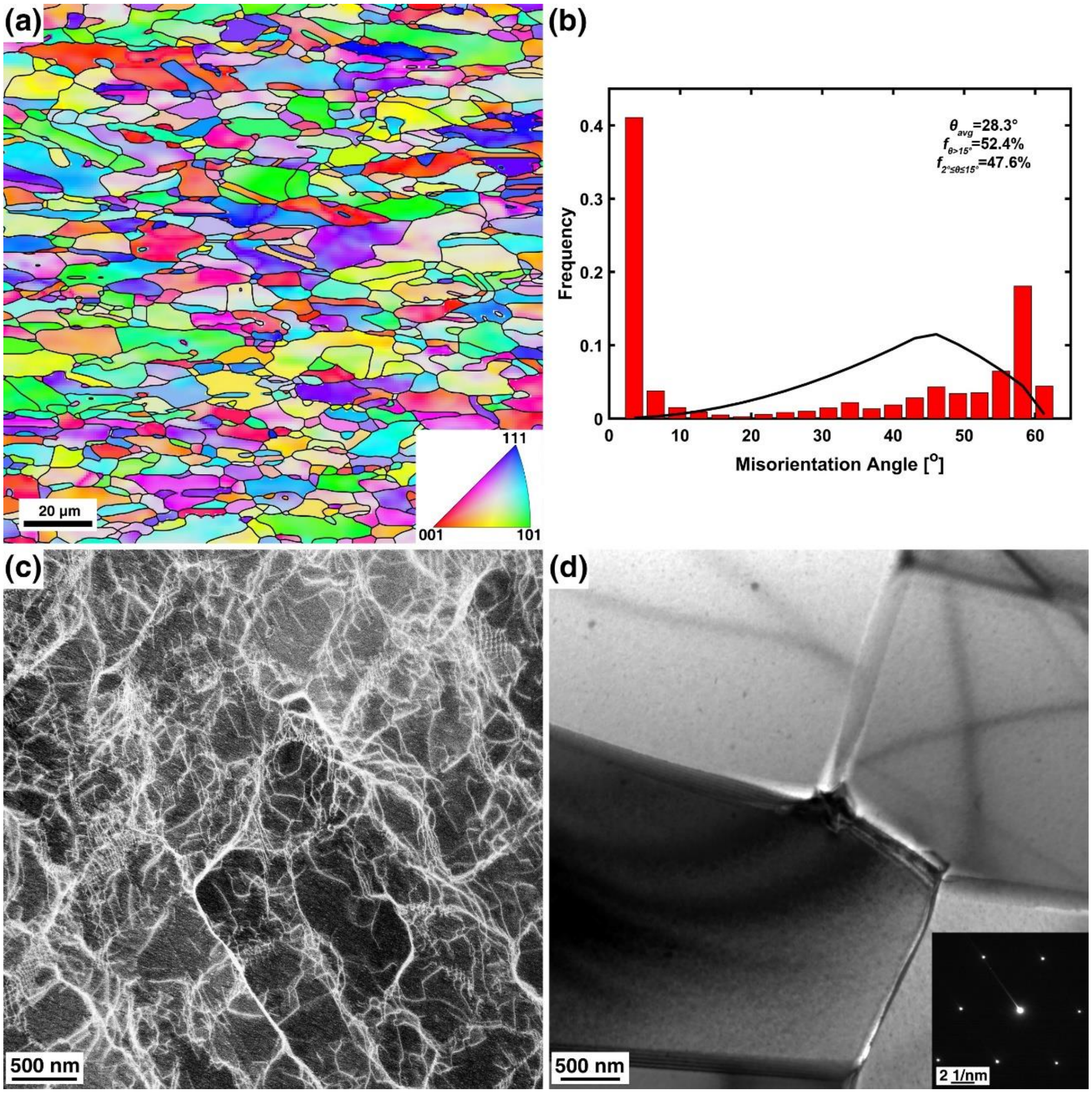

Fig. 2 The microstructure of the as-fabricated TWIP alloy: (a) typical IPF map; (b) grain misorientation distribution (The black line shows the random distribution misorientation); (c) HAADF-STEM image of a dislocation tangling zone and (d) typical bright field image and selected area diffraction pattern of a dislocation-free zone.

Table 1 Mechanical properties of the alloy deformed at different temperatures

Temperature (K)	σ_{YS} (MPa)	σ_{UTS} (MPa)	Total elongation	WHC ($\times10^{-3}$)
373	354	796	0.68	3.46
293	442	918	0.72	3.83
173	625	1107	0.54	4.33
77	760	1312	0.56	4.99

3.3 Diffraction data analysis

In situ neutron diffraction tests were carried out at four deformation temperatures (373, 293, 173 and 77 K). The normalized diffraction patterns during tensile testing at 373 and

77 K (axial detector) were plotted against the true stress in Fig. 4a and 4b, respectively. FCC austenite phase (γ) was confirmed to be the matrix phase and did not transform during cooling. The lattice parameter of the austenite phase versus temperature was determined by performing Rietveld refinement. The lattice parameter at 373 K is 3.619 Å and almost linearly decreases to 3.610 Å at 77 K (Table 2).

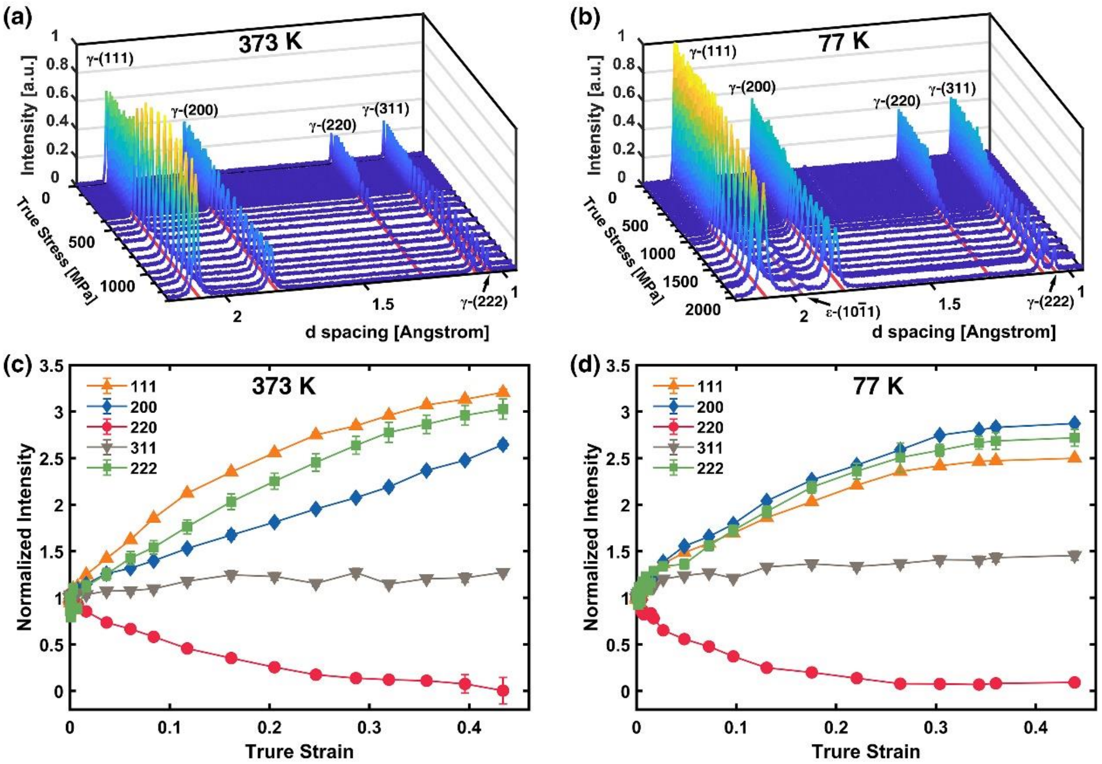

Fig. 4 Diffraction patterns with respect to true stress when deforming at (a) 373 K and (b) 77 K; Normalized intensity as a function of true strain at (c) 373 K and (d) 77 K.

The integrated intensity of each orientation during deforming at 373 and 77 K was normalized with that at undeformed state and plotted with strain in Fig. 4c and 4d, respectively. The texture is almost unchanged during elastic deformation, after which the evolution of each orientation varies due to the inherent anisotropy of the alloy. The intensity of γ-(111), γ-(222), γ-(200) peaks kept increasing, indicating grains with these orientations gradually rotated to tensile axis. Contrarily, the γ-(220) intensity decreased and γ-(311) changed only slightly since (220) grains rotated away from tensile axis while (311) grains are stable during straining. It is worth mentioning that the intensity curves at both temperatures appeared to stabilize at the end of the deformation while 77 K showed an earlier turning point than 373 K. The saturation of the texture indicates the limited dislocation behavior and activation of a new deformation mechanism. Besides, no new reflection peaks were found when deformation temperature is between 373 and 173 K, indicating that the structure of the alloy is stable and remained as FCC structure during deformation. While at 77 K, the intensity of all 5 reflection peaks of the γ phase decreased initially and stabilized at large strain conditions (>0.3). One new peak indexed as the $(10\bar{1}1)$

plane of the HCP phase [32] appeared. This shows that there is not only texture change but also FCC-to-HCP martensitic transition occurred during deformation at 77 K.

3.4 Lattice strain evolution

In Fig. 5, the lattice strain evolution of five grain families ({111}, {200}, {220},{311} and {222}) from axial and radial direction was plotted as a function of true stress at 373, 293, 173, and 77 K. The uncertainty of the measured strain is constrained to less than 30 microstrain [33]. Fig. 5a shows that at 373 K, the lattice strain curves from all crystallographic grain planes increased linearly with true stress up to its yielding point (354 MPa). Then a nonlinear relationship was observed at all crystallographic grain planes since the stress transferred from some stiff grain families (e.g., 220) to compliant grain families (e.g., 200) after yielding. Similar behavior was also observed at the other three temperatures, as shown in Fig.5b-5d. Besides, the maximum lattice strain values (both axial and radial directions) for all 5 grain planes increased with the dropping of deformation temperature.

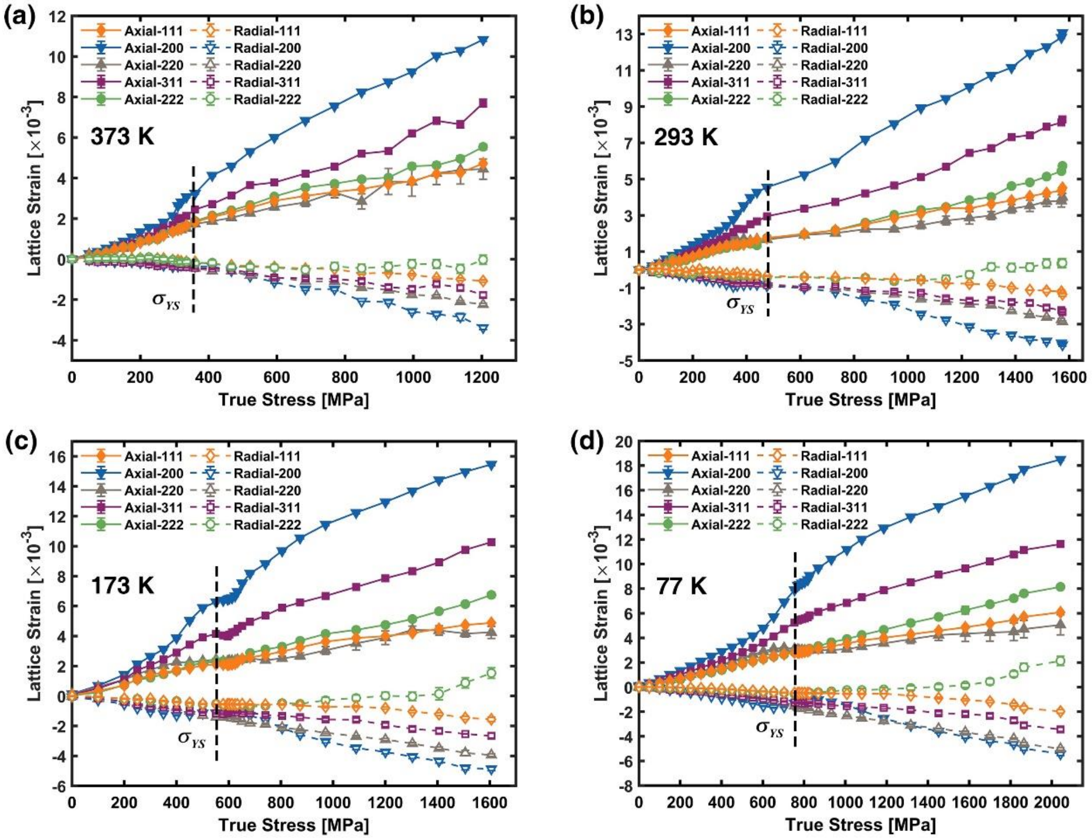

Fig. 5 Lattice strain curves of crystallographic planes {111}, {200}, {220}, {311} and {222} obtained from the axial and radial detectors during deforming at different temperatures: (a) 373 K (b) 293 K (c) 173 K and (d) 77 K.

The elastic constants at the tensile and compressive directions were obtained from the linear fitting of the lattice strain of axial and radial directions before the yielding of each grain plane (Fig. 5), respectively. The lattice parameter evolution with stress at radial and axial direction were determined with Rietveld refinement. At elastic stage, the lattice parameters at radial and axial directions increased and decreased linearly with true stress, respectively. Their slopes were linearly fitted to determine the tensile and compressive Young's modules. The ratio of the two were the Poisson's ratio (V). The shear modulus (G) was calculated via $G = E/2(1+V)$. The Poisson's ratio and shear modulus at different temperatures are shown in Table 2. Likewise, we determined the elastic constants of each orientation (E_{111}, E_{200}, E_{220} and E_{311}) as shown in Table 2. The ratio of elastic constants between the radial and axial directions was used to determine Poisson's ratios at each orientation. At all temperatures, E_{111} and E_{200} have the highest and lowest values, respectively. As the temperature decreasing, the stiffness of the alloy increased. E_{111} and E_{311} were enhanced while E_{200} and E_{220} remained at the same level. This phenomenon can be ascribed to the shrinkage of atomic bonds during temperature dropping [34].

Table 2 Various properties of the TWIP steel at different temperature

Temp. (K)	a_0 (Å)	E (GPa)	E_{111} (GPa)	E_{200} (GPa)	E_{220} (GPa)	E_{311} (GPa)	V	V_{111}	V_{200}	V_{220}	V_{311}	G GPa)	SFE (mJm-2)
77	3.610	179.4	258	131	203	171	0.257	0.207	0.344	0.284	0.289	71.4	17.2±1.1
173	3.613	179.8	243	130	195	158	0.261	0.181	0.321	0.271	0.273	71.3	21.7±1.1
293	3.616	179.9	235	129	191	156	0.267	0.176	0.317	0.257	0.251	71.0	30.5±1.3
373	3.619	179.7	225	138	203	154	0.284	0.166	0.292	0.256	0.229	70.2	34.8±1.6

3.5 SFP and SFE calculation

Many studies [19,22,33] demonstrated that stacking faults accumulation at FCC alloys can lead the shifting of two consecutive crystallographic grain planes (e.g., {111} and {222}) differently. Therefore, stacking fault probability (SFP), which evaluates the density of stacking faults, can be calculated by measuring the splitting distance between the lattice strain curves of {111} and {222}. Lattice strain curves of two successive grain families {111} and {222} at the four temperatures (373, 293, 173, and 77 K) were then plotted with respect to true strain in Fig. 6a-6d, respectively. Separation of lattice strain curves of {111} and {222} grain families at four deformation temperatures can be clearly observed, indicating the formation of stacking faults, which is used to calculate the SFP as follows.

To calculate the SPF, an equation considering the strain induced by macro-strain ($\varepsilon_{hkl}^{strain}$) and stacking faults ($\varepsilon_{hkl}^{sf}$) has been proposed in Ref.[5]:

$$\varepsilon_{hkl}^{exp} = \varepsilon_{hkl}^{strain} - \varepsilon_{hkl}^{sf} = \varepsilon_{hkl}^{strain} - \frac{\sqrt{3}}{4\pi}\frac{\sum b \pm \left(h+k+l\right)}{\left(u+b\right)\left(h^2+k^2+l^2\right)}SFP \tag{3}$$

,where u and b are the numbers of non-broadening and broadened components due to stacking faults [5]. Since successive grain families are equivalent in the crystallographic directions, their lattice strain change should be the same when only macro-strain is considered. Therefore, the SFP can be derived from the lattice strain of {111} and {222} via [5]:

$$SFP = \frac{32\pi}{3\sqrt{3}}\left(\varepsilon_{222}^{exp} - \varepsilon_{111}^{exp}\right) \tag{4}$$

The calculated SFP at different temperatures was plotted against strain in Fig. 6a-6d. SFP fluctuates at a very low level when the true strain is small. Sometimes the values are even negative, due to small errors induced by peak fitting. When SFP reached 0, they increased almost linearly with true strain. A linear equation was then fitted to the SFP versus true strain after considerable stacking faults have formed (when SFP is higher than 0.01). The slope of the fitted line of SFP (∂SFP/∂ε) indicates the speed of stacking fault formation, which was plotted against deformation temperature in Fig. 7a. It started from 3.3×10^{-2} at 373 K and almost linearly increased to 7.7×10^{-2} at 77 K. This indicates that stacking faults form much more quickly at cryogenic temperatures than at higher temperatures (e.g. 373 K).

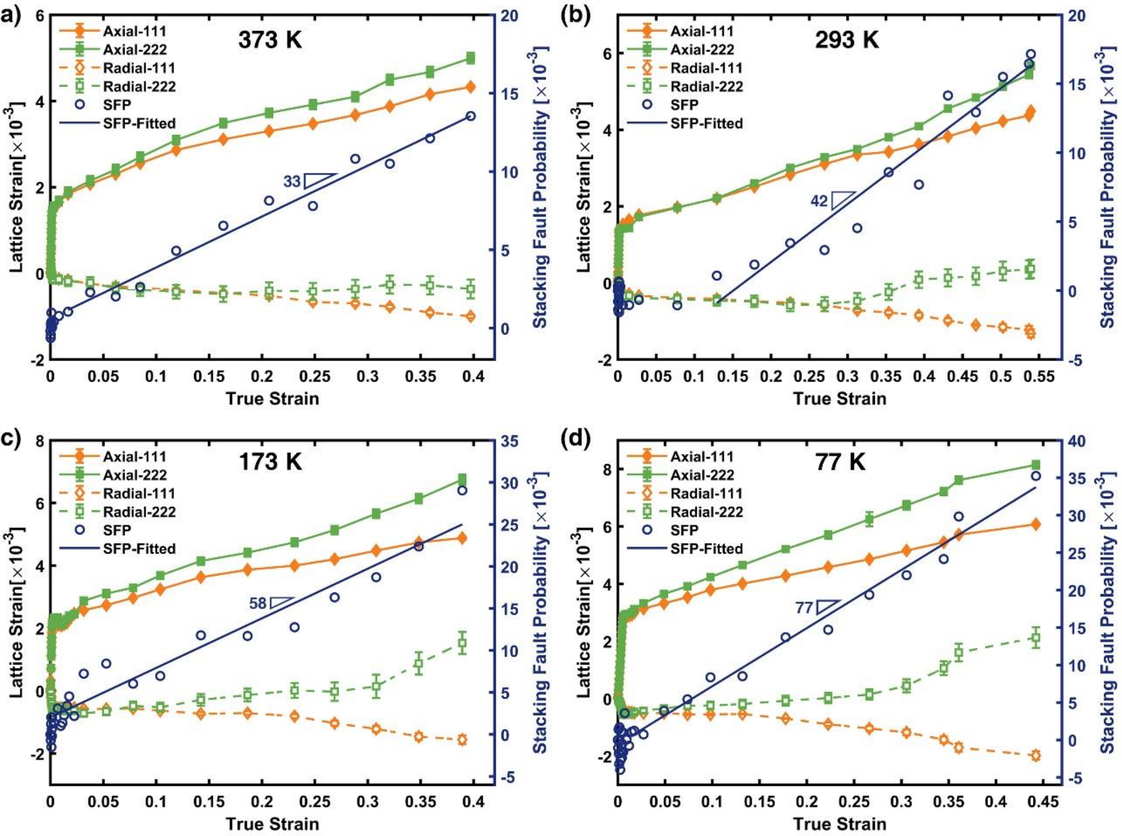

Fig. 6 Evolution of lattice strain and stacking fault probability as a function of true strain at different temperature: (a) 373 K, (b) 293 K, (c) 173 K and (d) 77 K.

According to Reed and Schramm [35], SFE measures the easiness of dissociation of a perfect dislocation into partial dislocations and creating stacking faults. The relationship between SPF and SFE is depicted with:

$$\gamma_{isf}=\frac{6.6a_0}{\pi\sqrt{3}}\frac{\langle\varepsilon^2\rangle_{111}}{SFP}\left(\frac{2C_{44}}{C_{11}-C_{12}}\right)^{-0.37}\left(\frac{C_{44}+C_{11}-C_{12}}{3}\right) \qquad (5)$$

, in which a_0 is the lattice parameter and γ_{isf} is the intrinsic stacking fault energy. The mean-square strain, $\langle\varepsilon^2\rangle_{111}$, was calculated by deconvoluting size and strain broadening effects with double-Voigt method [36]. The detailed procedure to calculate mean-square strain can be found in the Supplementary Material. The single crystal elastic constants (C_{11}, C_{12}, and C_{44}) of Fe-24wt%Mn-4wt%Cr alloy, a close composition to ours, were calculated based on the *ab initio* simulation results of Ref. [37]. It was found that C_{11}=222 GPa, C_{12}=159 GPa, and C_{44}=150 GPa. Single crystal elastic constants are temperature-dependent, but only vary slightly between 77 and 373 K [38–40]. The coefficient $\left(\frac{2C_{44}}{C_{11}-C_{12}}\right)^{-0.37}\left(\frac{C_{44}+C_{11}-C_{12}}{3}\right)$ in Eq. (5) is even less temperature sensitive within the temperature range according to our analysis on Fe [38], CrCoNi medium entropy alloy [40] and Cr-Mn-Fe-Co-Ni high-entropy alloy [41] (see the Supplementary Material). Here, we used single crystal elastic constants of Fe-24wt%Mn-4wt%Cr alloy at room temperature to estimate SFE of various temperatures using Eq. (5), as shown in Table 2. It is expected that a precise measurement of the single crystal elastic constants of the alloy as a function of temperatures via experiments and *ab initio* simulation could increase the accuracy of SFE calculation.

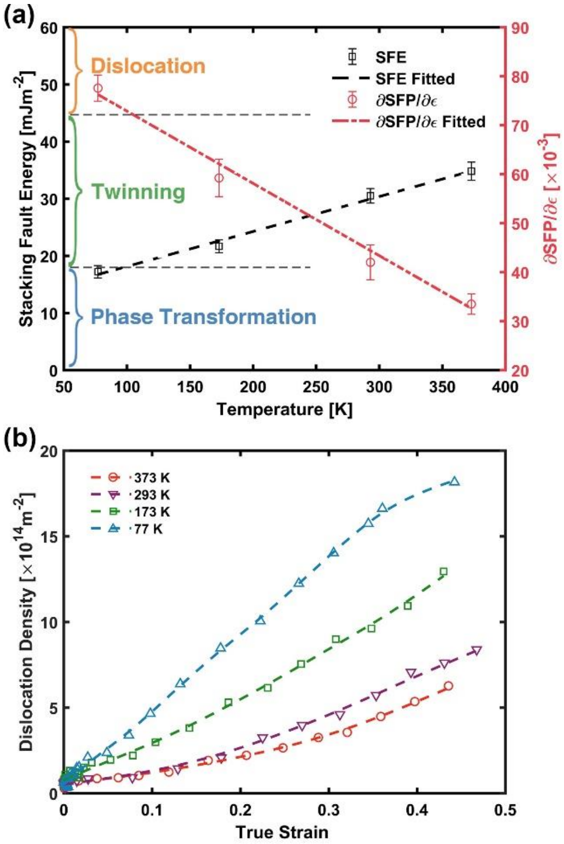

Fig. 7 (a) Temperature dependence of stacking fault probability and stacking fault energy and (b) dislocation density evolution with true strain at different temperatures.

The evolution of SFE with deformation temperature is shown in Table 2 and Fig. 7a. The different deformation mechanism regimes defined by SFE [11,12], as stated in the introduction, were overlapped in Fig. 7a. In our study, SFE of the alloy started from 34.8 mJm^{-2} at 373 K and almost linearly declined to 17.2 mJm^{-2} at 77 K. The linear relationship between SFE and temperature was also predicted by thermo-dynamic simulation [4] and first principle calculation [14]. According to Fig. 7a, for this alloy, twinning would occur and play an important role during deformation at all four temperatures. At 373 K, the SFE value was close to the regime boundary separating dislocation slipping and twinning, therefore, dislocation motion might be still the major deformation mechanism. As test temperature decreasing, the role of twinning became more pronounced. At 77 K, SFE dropped to the boundary of twinning and phase transformation, indicating that phase transformation could occur but at a low extent. This result agrees well with the highest SFP rate and the formation of HCP-ε phase at 77 K observed in neutron reflections (Fig. 4b).

3.6 Dislocation density evolution

To estimate the contribution of dislocation multiplication to the strength enhancement, a quantitatively analysis of dislocation density was necessary. Fig. 7b shows the calculated dislocation density (ρ) evolution during tensile testing at different test temperatures. Initially, the dislocation density at all temperatures was around 7×10^{13} m^{-2}, indicating that the fabrication processes induced pre-existing dislocations (Fig. 2c), which did not change significantly when temperature dropped. During elastic deformation, dislocation density did not change much. After yielding, the dislocation density increased with strain. Fig. 7b shows that the lower the deformation temperature, the higher the dislocation density at the same strain level. There appears to be a saturation period at high strain levels before failure at 77 K. Saturation of dislocation density was also observed in an Al-alloyed TWIP steel that the dislocation density saturated at 1×10^{15} m^{-2} at a strain of ~0.35 [42], which is of similar magnitude as ours. The highest dislocation density of 1.82×10^{15} m^{-2} was reached when deforming at 77 K to a true strain of 0.44, while the corresponding dislocation density was only 0.63×10^{15} m^{-2} at 373 K when deforming to a similar strain level. The dislocation density curves against strain between yielding and saturation appeared to be almost linear. By linearly fitting the curves, the slope of the fitted lines represents the increase rate of dislocation density (R_{dis}). At high temperatures, R_{dis} was low, about 1.1×10^{15} m^{-2} at 373 K and 1.6×10^{15} m^{-2} at 293 K. While it increased to 4.3×10^{15} m^{-2} when the test temperature was decreased to 77 K. Decreasing of test temperatures accelerated dislocation formation, especially at low strain conditions.

3.7 Microstructure characterization

Fig. 8 shows OM images taken from the fractured samples deformed at 293 and 77 K to different strain levels (~0.1, ~0.2 and ~0.3). When deformed at 293 K with a low strain of ~0.1 (Fig. 8a), twinning formation was inhomogeneous. Most of the grains were twin-free and only a very limited number of grains, which probably have preferred orientation for twinning, showed features of primary twinning. These twins were short and had a wide twin spacing. Similar phenomenon was also reported in [43], showing that twinning was preferably initiated from grains with orientations such as <111>//tensile axis, while the orientation, <001>//tensile axis, is much harder for twinning. De Cooman et al. [44] pointed out that mechanical twinning prefers to occur in grains with a high dislocation density. Our TEM observation shows that some grains of the as-fabricated sample have dense dislocation networks (Fig. 2c), at which twinning could prefer to occur firstly. With the increase of strain, these primary twins gradually occupied the grain interior and grew denser. Only very few secondary twinning can be observed at a strain of ~0.2 (Fig. 8b). Then twins propagated to other grains at higher strain conditions (Fig. 8c). Comparing with the situation at 293 K, twinning was more prominent at 77 K. At all three strain levels at 77 K, more grains were twined with a higher twin density. Meanwhile, there are more secondary twinning, intersecting with the primary twins when deforming at 77 K (Fig. 8d-8f). This is consistent with the measurement of SFP (Fig. 6). Since stacking faults serve as the embryo of twinning, SFP curves could be used to predict the formation of mechanical twins. Higher SFP was achieved at a lower temperature at a faster rate, hence, more mechanical twins are expected at 77 K than 293 K.

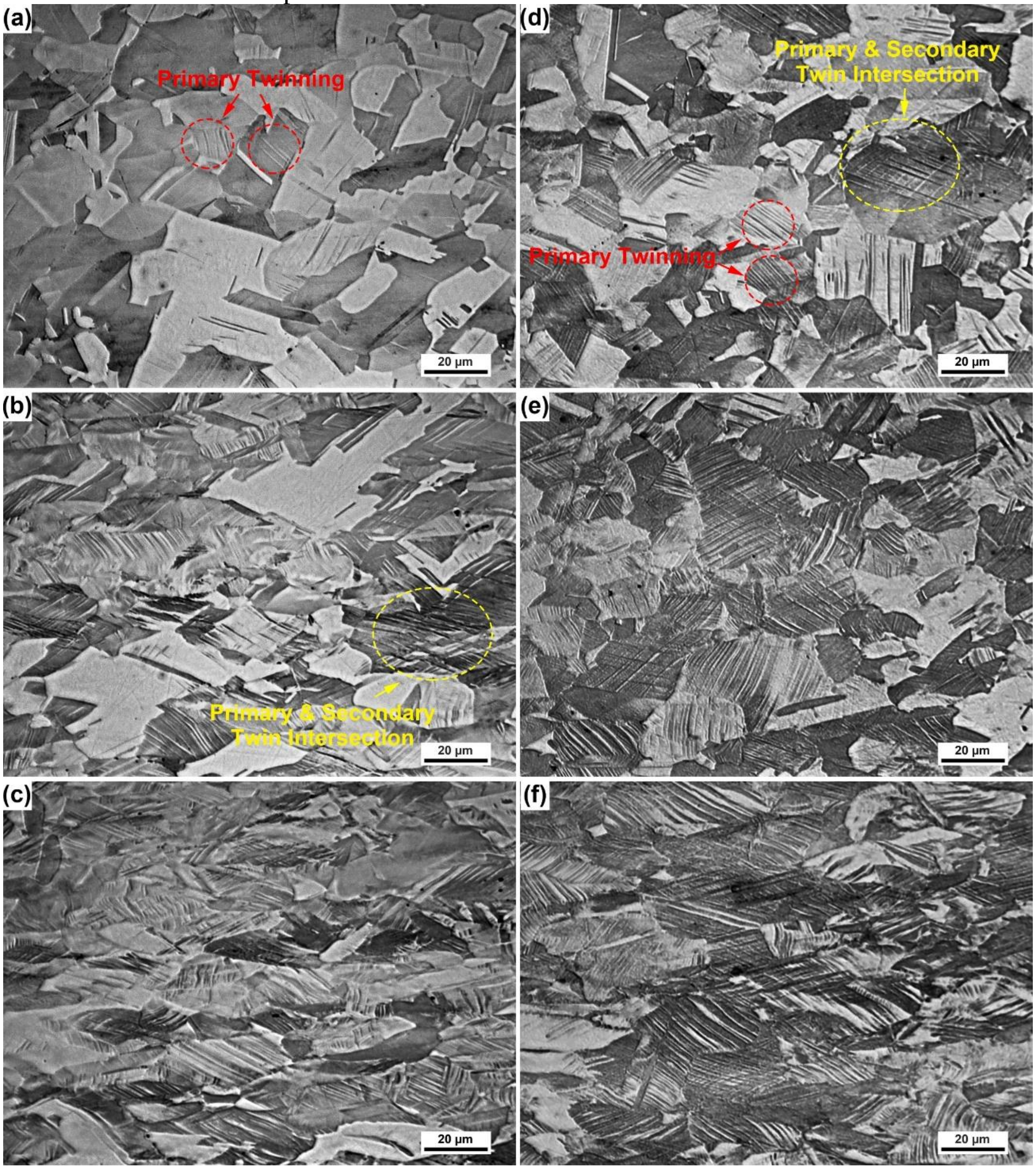

Fig. 8 Grain morphology observed by OM in TWIP steel deformed at 293 K and 77 K with different true strain: (a) 293 K, ε=~0.1; (b) 293 K, ε=~0.2; (c) 293 K, ε=~0.3; (d) 77 K, ε=~0.1; (e) 77 K, ε=~0.2; (f) 77 K, ε=~0.3.

To further investigate the twinning process at 77 K, high-resolution EBSD image quality maps were obtained at different strain levels of ~0.05, ~0.1 and ~0.2 (Fig. 9). Even with very a very small strain (~0.05, Fig.9a), most grains were dominated by dense primary twins or primary/secondary twin networks. The rectangle area in Fig. 9a was magnified in Fig. 9b. Primary and secondary twins were both observed at low strain level, which could benefit the formation of dense hierarchical twinning networks during subsequent straining. The propagation of twinning usually started from grain boundaries, implying that grain boundaries were the preferable nucleation locations for mechanical twins [45]. As shown in Fig. 9b, the primary twins were very thin and distributed discretely. Then the converge of multiple thin twins was also observed, forming one thick twinning band. As the strain raising to ~0.1, dense twinning networks consisting of thick twins formed and twins propagated to nearly every grain interior (Fig. 9c). When the strain reached ~0.2, more dense twinning networks were observed while some intersecting twinning networks, though very thin, also started to grow in grains with unfavorable orientations (as shown with the yellow circle in Fig. 9d).

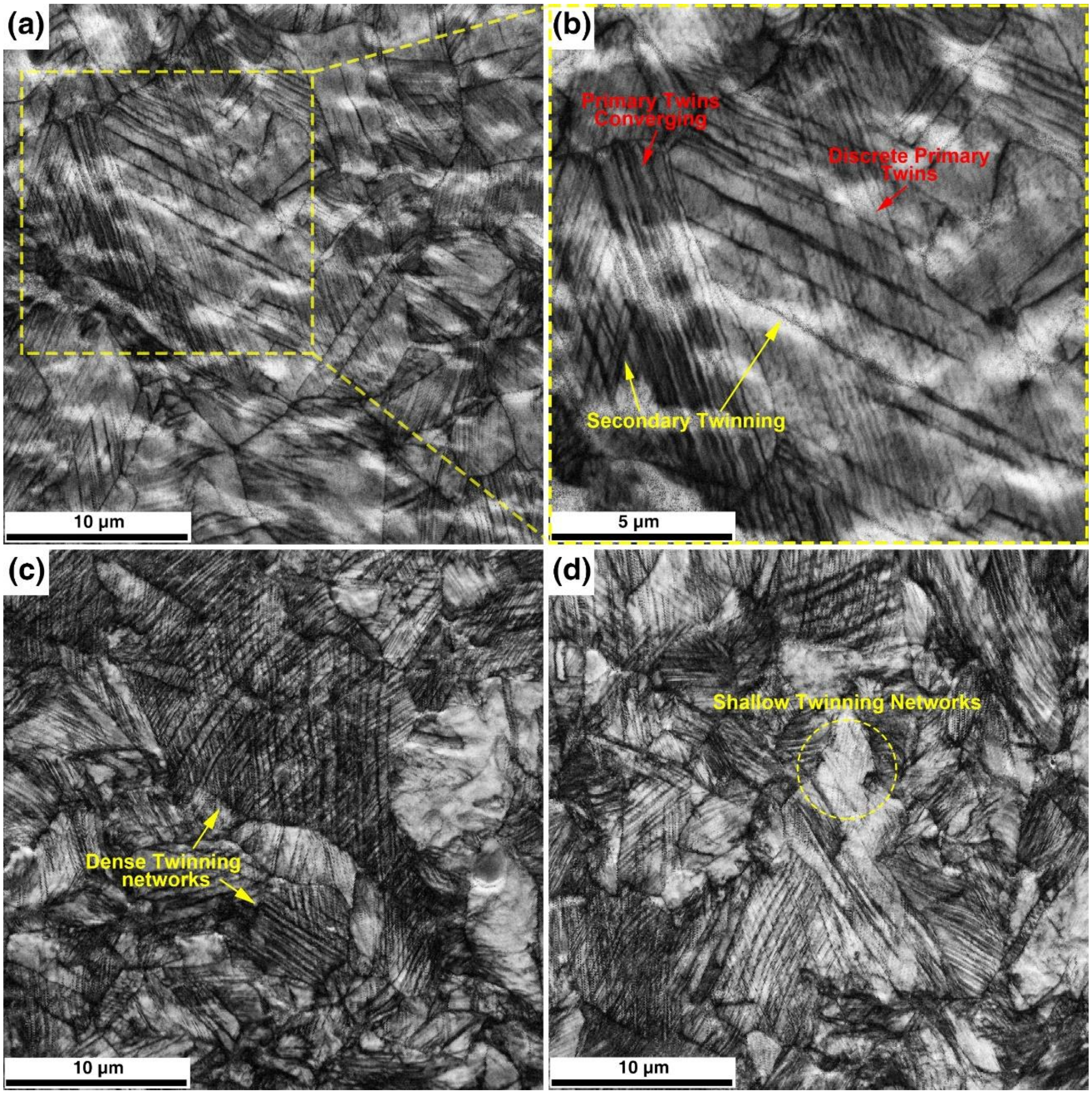

Fig. 9 EBSD image quality maps showing the twinning gathering process with increasing tensile strain at 77 K: (a) strain of 0.05; (b) higher magnification of the rectangle zone in (a); (c) strain of ~0.1; (d) strain of ~0.2.

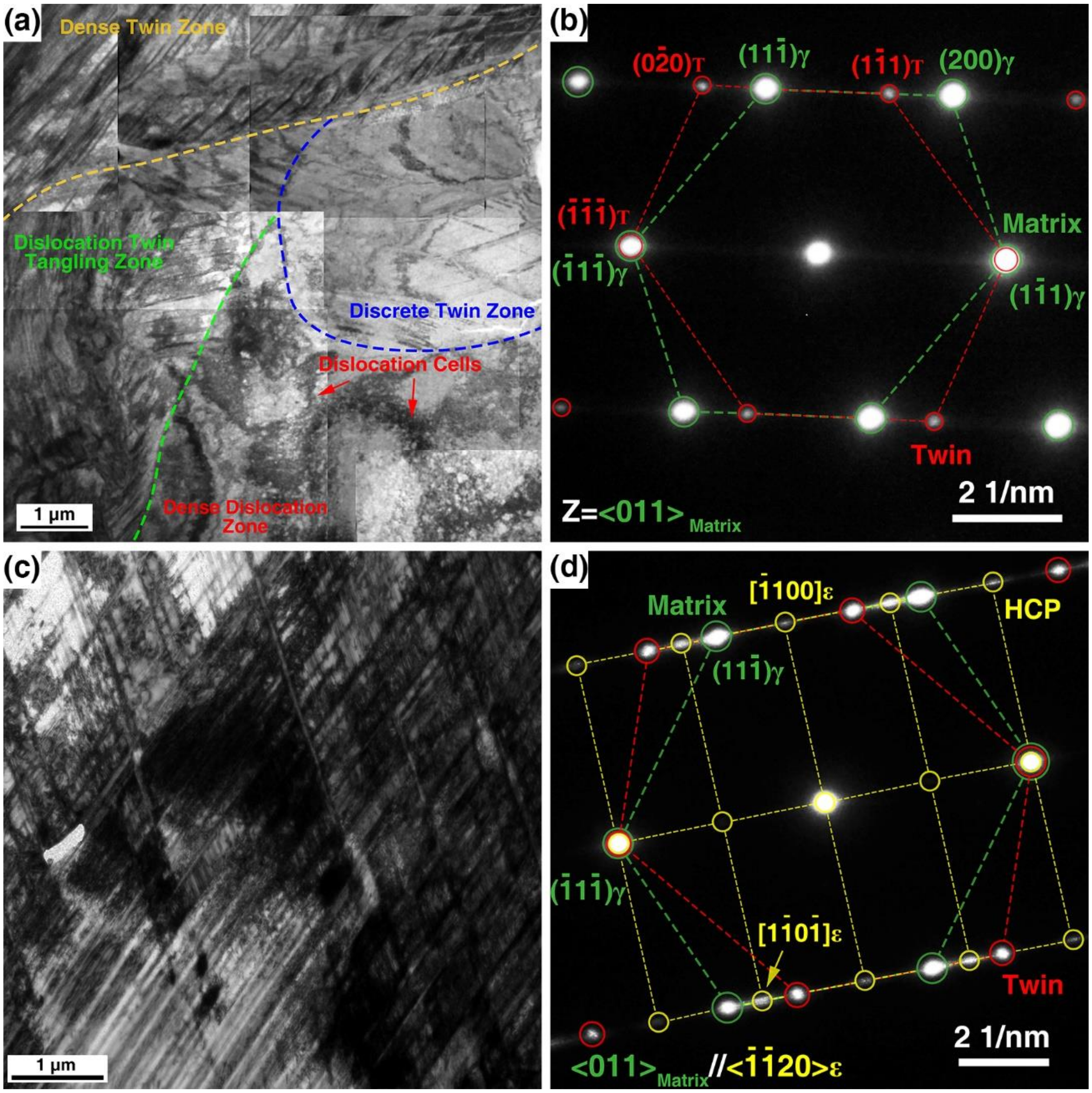

Fig. 10 TEM images taken from the sample deformed to true strain ~0.3 at 373 K and 77 K. (a and c) bright filed image at 373 K and 77 K, respectively; (b and d) SAED patterns of (a and c), respectively; shows that the twin density increases with the deformation temperature decreasing and FCC-γ to HCP-ε transition occurred at 77 K.

To further study the influence of temperature on the morphology of the twinning and dislocation, TEM examination was performed on samples deformed to ~0.3 strain at 373 and 77 K, as shown in Fig. 10. Twins were observed at both temperatures, which were confirmed by the twin reflections in the associated selected area diffraction patterns (SEAD) recorded along the <011> direction (Fig. 10b and 10d). Based on the distribution and density of twins and dislocations, Fig. 10a can be divided into four regions: (1) dense twin zone, (2) dislocation-twin tangling zone, (3) discrete twin zone, and (4) dense dislocation zone. At the dense twin region, massive nanosized twins were observed starting at grain boundaries and being prolongated through the grain interior. At the discrete twin zone, much less twins with a wide twin spacing (~600 nm) were formed. The dislocation-twin tangling zone shows the interaction between massive dislocations and twins, indicating that the dense twin boundaries act as columns trapping dislocations in between. In the dense dislocation zone, some grains remained as untwined and dislocation motion is still the main deformation mechanism, forming thick dislocation walls and large dislocation cells (~3 μm).

On the other hand, at 77 K the enhanced twinning activity led to hierarchical twin-twin intersections, trapping dense dislocation in intra-twin regions in Fig. 10c. This indicates more effective 3-dimentional twin networks were formed in impeding dislocation motion. Besides, phase transformation was confirmed by the SEAD pattern at 77 K (Fig. 10d). This is consistent with the previous results obtained from *in situ* neutron diffraction (Fig. 4b). The experimental result suggests the gradual transition of deformation behavior from dislocation motion to twin-twin/dislocation interaction and even to phase transformation as the test temperature dropped. This agrees well with the SFE-temperature map developed (Fig. 7a).

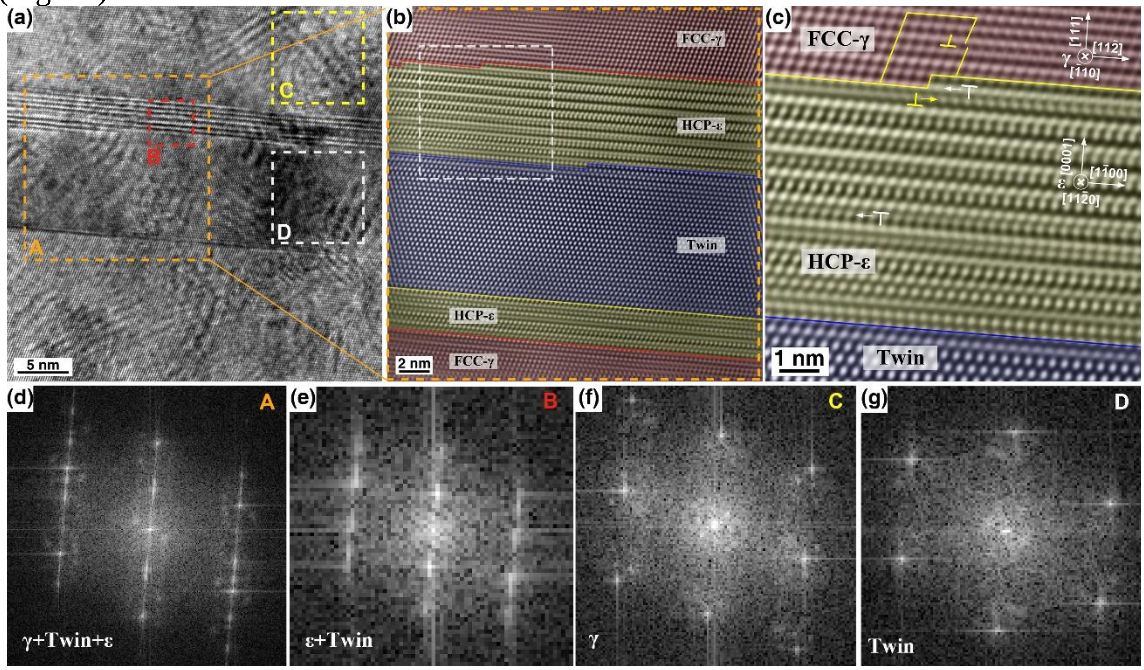

Fig. 11 Twinning formation and γ→ε phase transformation of the alloy during deformed at 77 K to a true strain of ~0.3: (a) HRTEM image; (b) atomic image of A area in (a); (c) higher magnification of the white rectangle areas in (b) and (d-g) FFT images at areas of A, B, C and D in (a).

The twin growth and martensite phase transformation (FCC-γ to HCP-ε) at 77 K were further revealed by HRTEM. The TEM sample was extracted from the failed sample at a strain of ~0.3. Fig. 11a-11c show the HRTEM images focusing on the γ/ε/twin interfaces, viewed along $[\bar{1}10]\gamma//[11\bar{2}0]\varepsilon$ directions. The fast Fourier transformation (FFT) images (shown in Fig. 10d-10g) were obtained from the marked areas in Fig. 11a, identifying the existence of twins and HCP-ε laths. In Fig. 11a, one nanosized twin with thickness of 9 nm was observed, as well as two HCP-ε laths (with width of 0.7 and 4 nm, respectively) locating at the twin-matrix interface. The rectangle area in Fig. 11b was magnified in Fig. 11c, which shows that several Shockley partial dislocations with different Burger's vectors glided at the edge of HCP-ε laths, creating new stacking faults and leaving HCP-ε laths behind. These results indicate that the FCC-γ to HCP-ε phase transformation preferably occurs at the twin boundaries and the two microstructural features (twinning and phase transformation) are closely related to perfect dislocations dissociation, following (partial) dislocation reaction and related stacking faults motion. The interaction of two leading partials of two stacking faults on two {111} grain plane can create a stair-rod dislocation via:

$$\frac{a}{6}[2\bar{1}\bar{1}]+\frac{a}{6}[\bar{1}21]\rightarrow\frac{a}{6}[110] \tag{6}$$

The new-born stair-rod dislocation is sessile and can serve as Lomer-Cottrel lock [46] since its Burgers vector is perpendicular to the dislocation line and does not lie on the two {111} planes of the adjacent stacking faults [47]. According to Ref. [48], the Shockley partial dislocations ($b:\frac{a}{6}[\bar{1}21](111)\gamma$) could interact with perfect dislocations ($b:\frac{a}{2}[10\bar{1}](111)\gamma$) during their movement and create straight Frank sessile dislocations ($b:\frac{a}{3}[11\bar{1}](111)\gamma$) lying at the twin-matrix interface. These dense Frank dislocations can affect the dynamic of the twinning and twin boundary expansion, maintaining the high stability of twins and making twin boundaries hard to be penetrated by dislocations. On the other hand, the partial dislocation motion and the new-born stacking faults also play a decisive role in mechanical twin formation and martensite phase transformation. X. Yang et al. [49] proposed three types of partial dislocations and indicated that the mechanical (de)twinning is caused by gliding one partial dislocation on consecutive (111)γ planes. Regarding to martensitic phase transformation, when partial dislocations glide from plane B and consecutively on every second (111)γ planes, the parent stacking sequence of …ABCABC…(FCC-γ matrix) will transfer into …ACACAC…(HCP-ε laths). These HCP laths preferably initiate at the interface of twin-matrix. Similar phenomena were also found at other TWIP steels [4,50], where the expansion and growth of HCP laths gradually fulfilled the intra-twin regions.

In summary, the microstructure evolution observed at different temperatures agrees well with the neutron diffraction results (Fig. 4) and SFE-deformation mechanism evolution map (Fig. 7a). At high-temperature regime (e.g. 373 K), intensive dislocation motion and multiplication played a major role in accommodating strain due to its high SFE. Twinning induced hardening was not significant until reaching very high strain conditions. As the test temperature drops, SFE decreases, dislocation preferably to dissociate rather than glide to cater to plastic straining. This enables massive partial dislocation motion and rapid SFs formation (i.e. higher SFP rate, Fig. 7a), making twinning a more favorable deformation mechanism at cryogenic conditions. When SFE is low enough (e.g. 18.3 mJ/m^{-2} at 77 K) phase transformation from parent FCC phase to HCP laths can be triggered.

4. Discussion

In the following, the dependence of yield strength (Fig. 3b) and the contribution of dislocation and twinning to flow stress (Fig. 3c) will be discussed with dislocation slip system driven modelling.

4.1 Temperature dependent yielding strength

The yield point corresponds to the initiation of macroscopic unpinning and gliding of mobile dislocations. As show in Fig. 3a and 3b, σ_{YS} of the alloy was linearly enhanced by dropping deformation temperature. Prior to the detailed analysis of the temperature dependence of σ_{YS}, it is important to classify the strengthening contributors towards yielding strength. Generally, σ_{YS} is the result of the synergetic effects of multiple strengthening effects which can be decomposed into athermal ($\sigma_{Athermal}$) and thermal ($\sigma_{Thermal}$) parts:

$$\sigma_{YS} = \sigma_{Athermal} + \sigma_{Thermal} \tag{7}$$

The athermal component is generally related to strengthening resources of a long-range order (> 10 Å), such as initial dislocation density (σ_{dis}), precipitate hardening (σ_{PP}) and grain boundary hardening (σ_{GB}). In our case, the contribution from precipitates (σ_{PP}) can be ignored since the SEAD pattern (Fig. 2d) and the neutron diffraction spectra (Fig. 4) did not show the presence of precipitates, and the alloy remained single-phases (FCC) before yielding. Therefore, $\sigma_{Athermal}$ is determined from the rest two resources: initial dislocation density and grain boundaries.

The hardening effect from dislocation (σ_{dis}) can be calculated with Taylor equation [51]:

$$\sigma_{dis} = M\alpha Gb\rho^{1/2} \tag{8}$$

, in which M=3.06 is the Taylor factor, α is a constant for scaling the inter action strength between dislocations and a value of 0.26 was used here [52–54]. It is noted that different α values have been used in TWIP steels, such as 0.136 [25], 0.26 [52,53], and 0.4 [55]. We will show later that α=0.26 is a reasonable value for our TWIP steel. The temperature dependence of Burger's vector (b) has been ignored since the lattice parameter decreases only slightly during cooling down (Fig. 12a). The dislocation density of the as-fabricated state (7×10^{13} m^{-2}) was used and strength contribution from initial dislocations (σ_{dis}^{0}) was estimated to be 124 MPa.

The contribution from grain boundaries was calculated with the classical Hall-Petch formula [56] in which the strength contribution keeps a linear relationship with the inverse square root of average grain size (d):

$$\sigma_{GB} = K_{GB}d^{-1/2} \tag{9}$$

Hall-Petch coefficient (K_{GB}) of 0.357 MPa·m$^{0.5}$ was used based on Ref. [57], yielding the strength improvement from grain boundaries to be 95 MPa.

Meanwhile, barriers inhibiting dislocation gliding in a short range (< 10 Å) can give a rise to the thermal part of Eq .(7) [58]. It mainly derives from the thermally initiated dislocation gliding overcoming Peierls lattice potential friction and the pinning effect from solid solution atoms (e.g. carbon) [31,59]. Decreasing temperature can reduce atom vibration frequency and consequently increase the critical stress for the initiation of dislocation gliding. The strain rate $\dot{\varepsilon}$ can be expressed by Arrhenius relationship [60]:

$$\dot{\varepsilon} = \dot{\varepsilon}_0 \cdot \exp\left(\frac{\Delta G}{kT}\right) \tag{10}$$

, where $\dot{\varepsilon}_0$ is the reference strain rate and a value of 10^8 s^{-1} was assumed according to Ref. [61], k is the Boltzmann constant. ΔG is the free energy of overcoming barriers and can be well described with a phenomenological relation [60]:

$$\Delta G = Gb^3 g_0 \left[1 - \left(\frac{\sigma_{Thermal}}{\sigma_0} \cdot \frac{G_0}{G_T}\right)^p\right]^q \tag{11}$$

,where G_0 and G_T is the shear modulus of the alloy at 0 K and at temperature T, p and q are two constants describing the characteristics of the obstacles, g_0 is a scaling factor and a material constant, σ_0 is the mechanical threshold stress to overcome the lattice friction without thermal activation at 0 K. The temperature dependence of the shear modulus was fitted with an equation proposed by Y. P. Varshni [62]:

$$G_T = G_0 - A/\left[\exp(B/T) - 1\right] \tag{12}$$

The two adjustable parameters (A and B) were determined to be 77.5 and 1574, respectively, by fitting the shear modulus versus temperature curve (Fig. 12a). G_0 of 71.36 GPa was obtained by extrapolating Eq. (12) to 0 K (Fig. 12a). Similar temperature dependence of shear modulus of three Fe–18Mn–0.6C–xAl TWIP steels was reported in Ref. [31], where the shear modulus is slightly higher than our study. Combining the Eq. (10) and (11) yields the relationship between deformation temperature and $\sigma_{Thermal}$:

$$\sigma_{Thermal} = \sigma_0 \left(\frac{G_T}{G_0}\right)\left[1 - \left(\frac{kT}{g_0 G_T b^3} \ln\frac{\dot{\varepsilon}_0}{\dot{\varepsilon}}\right)^{\frac{1}{q}}\right]^{\frac{1}{p}} \tag{13}$$

This indicates the mechanical threshold value at 0 K, σ_0 can be decreased by the increasing thermal activation as a result of temperature rising. The strain rate is 9 × 10^{-4} s^{-1} in the present study and the two constants (p and q) were set to be 0.5 and 1.5 [63], respectively. Therefore, the normalized temperature-related component $\left(\frac{\sigma_{Thermal}}{G_T}\right)^p$ of σ_{YS} and normalized temperature $\left(\frac{kT}{G_T b^3} \ln\frac{\dot{\varepsilon}_0}{\dot{\varepsilon}}\right)^{\frac{1}{q}}$ was linearly fitted in Fig.12b. All measured data points can be well fitted into a line, indicating that the high temperature sensitivity of the σ_{YS} (Fig. 3b) originates from the increase in the lattice friction stress which is estimated to be 898 MPa at 0 K by extrapolating the fitted straight line to 0 K (Fig.12b). Temperature sensitivity of σ_{YS} observed in our study is very similar with that in [59], where the effect of carbon content is emphasized. The thermal component of a TWIP steel with 0.6% C can be significantly improved by ~350 MPa (which is 318 MPa in our case) when decreasing temperature from room temperature to 77 K.

In summary, the strengthening contributions to yield strength from different sources were calculated. The contribution from grain boundary was 95 MPa at all tested temperatures. The contribution from dislocations was 124 MPa. The lattice friction stress increased from

135 MPa to 541 MPa as the deformation temperature dropped from 373 K to 77 K, which is the main reason for the increase of yield strength at lower test temperatures.

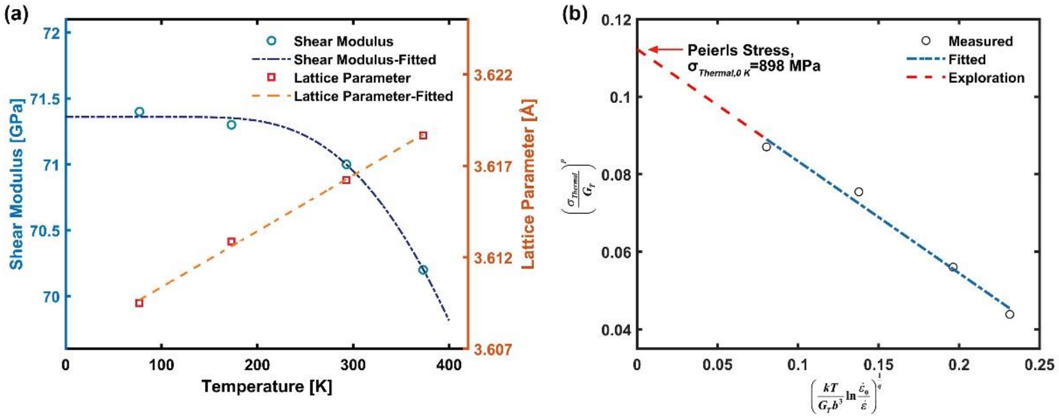

Fig .12 (a) Temperature dependence of the shear modulus and lattice parameter of the alloy and (b) normalized thermally activated component of the yielding stress with respect to the normalized temperature.

4.2 Plastic Deformation

At the plastic stage, in addition to grain boundary strengthening and lattice friction stress (σ_f), there are two additional contributors to the flow stress: (1) dislocation multiplication, and (2) twinning formation, and martensite phase transformation. The strengthening effect from dislocation density (σ_{dis}) can be calculated using Eq. (8). The dislocation density was measured from the *in situ* neutron diffraction pattern shown in Fig. 7b. This allows us to calculate σ_{dis} as a function of strain (e.g. Fig. 13a at 77 K) using Eq. (8). With regarding to phase transformation, the fraction of transformed HCP-ε laths is very small and are prone to locate at the twinning boundaries (Fig. 4b and 11). Meanwhile, stand-alone HCP-laths have a wide spacing distance and thin thickness (<5 nm), leading to very limited ability of impeding dislocation motion and thus low contribution towards strength [64]. Hence, we ignored the contribution from phase transformation. Therefore, the strengthening contribution from twinning (σ_{twin}) can be calculated indirectly as follows:

$$\sigma_{twin} = \sigma - \sigma_f - \sigma_{GB} - \sigma_{dis} \tag{14}$$

, where σ is the measured true stress. σ_{twin} versa true strain at 77 K was plotted in Fig. 13a. Alternatively, twin boundaries act as grain boundaries and its strengthening effect can be calculated with the Hall-Petch model directly [64]:

$$\sigma_{twin} = FK_{twin} l^{-0.5} \tag{15}$$

where F is the volume fraction of twins, l is the twin spacing, K_{twin} is the Hall-Petch coefficient of twinning. According to Refs. [65,66], the Hall-Petch constant for twinning is about equal to that for slip in Fe-22Mn-0.6C TWIP steel. In our study, K_{twin} is also assumed to be the same as K_{GB} [1]. This value has been widely used to model twin contribution to strength of TWIP steels with different compositions (e.g. in Refs. [67–69]) with great success. Another study by Kusakin et al. [70] shows that K_{GB} =0.35 MPa·m$^{0.5}$ via data fitting of various TWIP steels, which is close to 0.357 MPa·m$^{0.5}$ used by De las Cuevas et al. [57] and those reported in Cr-Ni austenitic steels [71]. Therefore, we used K_{twin} =0.357 MPa·m$^{0.5}$. F can be estimated with the stereological analysis of Fullman [72]:

$$\frac{1}{l} = \frac{1}{2e}\frac{F}{1-F} \tag{16}$$

in which e is the thickness of twins. Twin boundary density is usually calculated from TEM [52,73] or SEM [74] images. Based on TEM images, l was measured to be 212 nm and e was 95 nm when strain was ~0.2 at 77 K. With strain increased to ~0.3, twin spacing distance decreased to 153 nm and their thickness increased to 110 nm. Based on Eq. (15) and (16), F was equivalent to 0.474 and 0.589 at strains of ~0.2 and ~0.3, yielding the twin contribution of 376 and 538 MPa, respectively. In Fig. 13a, twinning contribution calculated from TEM images at true strain of 0.2 and 0.3 was compared with the indirect calculation with Eq. (14). The two methods agree very well.

As we stated before, various α values were used in Eq. (8) in literature, among which, we chose to use α = 0.26. This also allows us to verify the use of α = 0.26 in our study. The stress level after yielding can be predicted by Eq. (17):

$$\sigma_{\text{mod}} = \sigma_{twin} + \sigma_{dis}^{\varepsilon} - \sigma_{dis}^{0} + \sigma_{YS} \tag{17}$$

, in which σ_{mod} is the predicted flow stress. $\sigma_{dis}^{\varepsilon}$ is the strengthening contribution from dislocations at strain ε, while σ_{dis}^{0} is the strengthening contribution from initial dislocations in the as-received sample, both of which can be calculated from Eq. (8). The difference (σ_{diff}) between experimental measured stress (σ_{exp}) and modelling results (σ_{mod}) can be calculated by Eq. (18):

$$\sigma_{diff} = |\sigma_{\text{exp}} - \sigma_{\text{mod}}| \tag{18}$$

Combining Eq. (8), (15), (17) and (18), we can determine σ_{diff} with different α values as shown in Table 3. When α=0.26, σ_{diff} is the smallest among the three commonly used α values.

Table 3. σ_{diff} at two strain levels using different α values

K_{twin} (MPa·m$^{0.5}$)	α	Strain	σ_{diff} (MPa)
0.357	0.136	0.2	88.1
0.357	0.136	0.3	167.0
0.357	0.26	0.2	65.3
0.357	0.26	0.3	33.1
0.357	0.4	0.2	238.7
0.357	0.4	0.3	259.0

Fig. 13a displays the contribution from various strengthening resources at 77 K, showing the growing strength enhancement from both twinning (σ_{twin}) and dislocation (σ_{dis}) as the plastic strain increasing. Twinning contribution was not significant at low strain due to its low density. However, during tensile deformation, it increased faster than dislocations contribution. Twinning gradually became a comparable strengthening resource as dislocations at very large strain (higher than around 0.4). When strain reached 0.34, 507 MPa was from twinning while dislocations contributed 574 MPa. This phenomenon can be ascribed to that the dynamic recovery curbed dislocation multiplication at high strain conditions even at an extremely low temperature of 77 K, but nano-twins continuously increased during the deformation of the low-SFE TWIP steel.

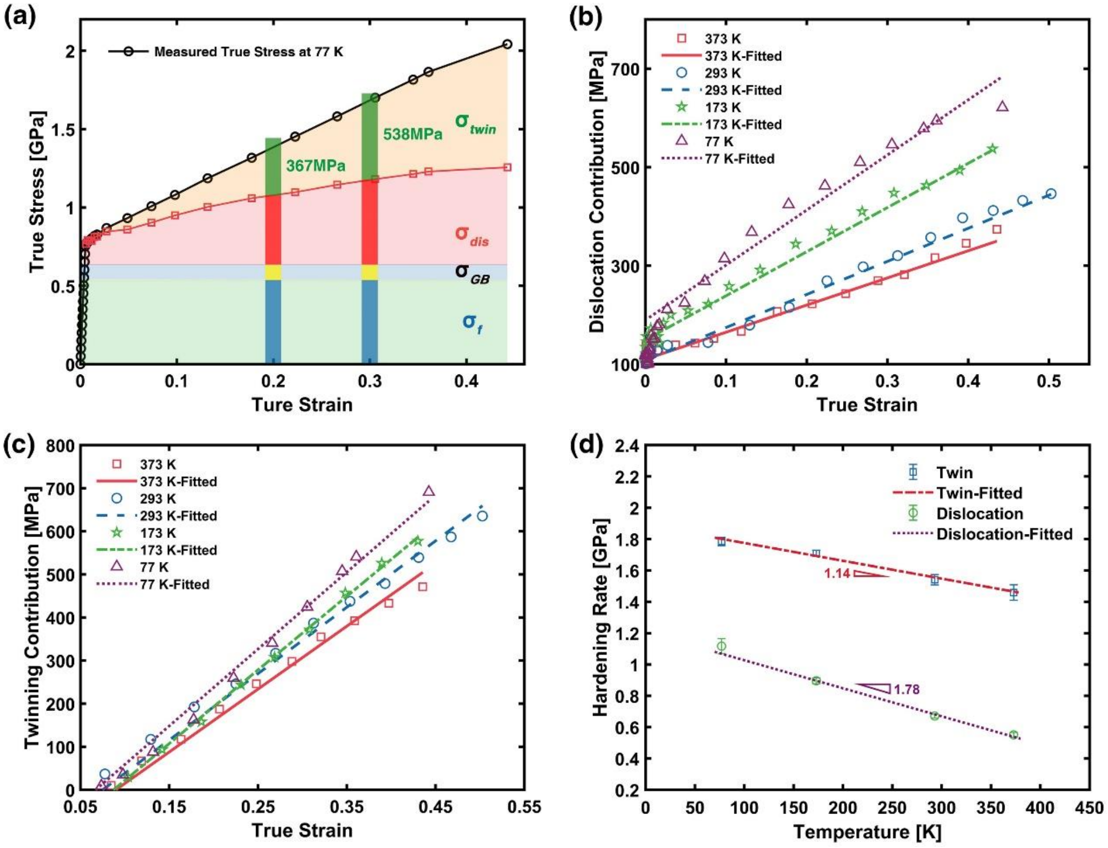

Fig. 13 (a) The respective contribution of multiple resources to the total flow stress; strain hardening contribution from (b) dislocation and (c) twin density at different temperatures; (d) temperature dependence of the hardening rate from dislocation and twinning.

The strengthening contributions from dislocations and twins at different temperatures were plotted against true strain in Fig. 13b and 13c, respectively. Due to the pre-existing dislocations, dislocation contribution started from at around 124 MPa for all 4 temperatures. It increased almost linearly with strain after yielding. The curves were fitted with linear functions and the slopes of the fitted lines were defined as dislocation-induced hardening rate ($\partial\sigma_{dis}/\partial\varepsilon$). Twinning contribution was also shown to be linearly increasing with true strain (Fig. 13c). Similarly, the slope of the fitted line is defined as twinning-induced hardening rate ($\partial\sigma_{twin}/\partial\varepsilon$). These two figures show a synergetic hardening mode of twinning and dislocation at the low-temperature range (from 373 to 77 K). The strain hardening capacity of this TWIP steel comes from both dislocation-induced hardening and twining-induced hardening. As the deformation temperature decreased, the strengthening contributions from dislocation and twinning both increased. On the one hand, temperature dropping inhibited some thermally activated processes (such as thermally driven cross-slip) and dynamic recovery [75], maintaining a high level of dislocation density and slowing down dislocation motion. Thus, the dislocation capacity (the maximum dislocation density) can be improved, achieving higher strengthening effects. On the other hand, a growing number of twins was produced as the SFE was reduced from 34.8 mJm^{-2} at 373 K to 17.2

mJm^{-2} at 77 K. It is also worth noting that although the twinning contribution at 293 K is less significant than at 77 K, it still grew rapidly with strain and contribute significant to strength: 316 MPa is from dislocations while twins contributed 394 MPa at strain of 0.36. This is in contrary with Ref. [25], where the twinning contribution to flow stress at 293 K is small and almost constant during deformation. This can be ascribed to the different compositions of the two TWIP steels and therefore the disparity in SFE. Meanwhile, the ductility of the alloy was decreased from 0.72 at 293 K to 0.56 at 77 K even with multiple strengthening mechanisms activated. The massive dislocations and twinning boundaries can bring high strength by providing dense new dislocation motion barriers. However, the high density of barriers can evolve into dislocation walls, new-born phases [76] and the intersection of twinning [77], which can significantly increase the internal stress and serve as weak positions for crack initialization, hence reducing the ductility. Similar phenomenon can also be found at Ref. [78].

Fig. 13d shows the hardening rates of twinning and dislocation as a function of temperatures, interestingly, both of which show an almost linear relationship with respect to deformation temperature. Therefore, their relationship can be described as:

$$\frac{\partial \sigma_{dis}}{\partial \varepsilon \partial T} = -m_{dis} \tag{19}$$

$$\frac{\partial \sigma_{twin}}{\partial \varepsilon \partial T} = -m_{twin} \tag{20}$$

, where m_{dis} and m_{twin} are slopes of the hardening rate curves of dislocation and twinning respectively. With the help of linear curve fitting, m_{dis} was found to be about 1.78 $MPa\cdot K^{-1}$, which is higher than m_{twin} =1.14 $MPa\cdot K^{-1}$. The reason why the hardening rates of twinning and dislocation versus temperatures are both linear is unclear. This could be related to the linear relationship between SFE and temperature (Fig. 7a). More work would be needed to verify this observation on other alloys with TWIP effect. If validated, new analytic and numerical models could be developed to predict the flow stress evolution of TWIP alloys.

5. Conclusions

In this study we investigated the temperature dependence of the deformation mechanisms operating in a high Mn TWIP steel (Fe-24Mn-4Cr-0.5Cu-0.5C). *In situ* neutron diffraction was employed to map the evolution of multiple microstructure features (e.g., lattice strain, stacking fault probability, stacking fault energy and dislocation density) and record real-time mechanical responses. The microstructures evolution was then confirmed via post-mortem microscopy characterization. The investigation leads to the following conclusions:

(1) A steady increase in the tensile strength was observed as the test temperature dropped, maintaining high ductility (over 50%). The superior combination of engineering tensile strength (σ_{YS} of 760 MPa, σ_{UTS} of 1312 MPa) was obtained at 77 K, which is significantly higher than that at 373 K (σ_{YS} of 354 MPa, σ_{UTS} of 796 MPa).

(2) Via *in situ* neutron diffraction measurement, the stacking fault probability at different strain conditions was calculated. It increased almost linearly with the strain. Its increase rate became higher at lower test temperatures.

(3) SFE values of the alloy as a function of temperature were estimated, which was 34.8 mJm^{-2} at 373 K and decreased to 17.2 mJm^{-2} at 77 K, resulting in significant increase in twin density and even triggering martensitic transformation from FCC-γ to HCP-ε at 77 K.

(4) The dislocation density evolution was calculated using the modified Williamson-Hall method. The as-fabricated samples had a dislocation density of around 7×10^{13} m^{-2}. The dislocation density increased during tensile straining after yielding. Its rate of increase was higher at lower temperatures. The maximum value of 1.82×10^{15} m^{-2} was obtained when deforming at 77 K with true strain of 0.44.

(5) The respective contributions the flow stress from twins, dislocations, grain boundaries and solid solution during elastic, and plastic deformation were calculated. The increase of yield strength at lower temperatures was due to a significant increase of lattice friction stress (from 135 MPa at 373 K to 541 MPa at 77 K).

(6) During plastic deformation, dislocation hardening and TWIP effects worked synergistically in addition to grain boundary and solute strengthening. With very high strain hardening rate, the strength contribution form twinning increases rapidly, making twinning becomes a comparable strength contributor of dislocations at large strain conditions.

Acknowledgement

The authors thank ISIS neutron and muon source (the Rutherford Appleton Laboratory, UK) for providing the beamtime (RB1810732 and RB1920111) and staff at ENGIN-X beamline for help. BC acknowledges the support from the Diamond-Birmingham Collaboration.

References

[1] J.G. Kim, N.A. Enikeev, J.B. Seol, M.M. Abramova, M. V Karavaeva, R.Z. Valiev, C.G. Park, H.S. Kim, Superior Strength and Multiple Strengthening Mechanisms in Nanocrystalline TWIP Steel, Sci. Rep. 8 (2018). https://doi.org/10.1038/s41598-018-29632-y.

[2] B.C. De Cooman, Y. Estrin, S.K. Kim, Twinning-induced plasticity (TWIP) steels, Acta Mater. 142 (2018) 283–362. https://doi.org/10.1016/j.actamat.2017.06.046.

[3] S. Curtze, V.-T.T. Kuokkala, Dependence of tensile deformation behavior of TWIP steels on stacking fault energy, temperature and strain rate, Acta Mater. 58 (2010) 5129–5141. https://doi.org/https://doi.org/10.1016/j.actamat.2010.05.049.

[4] Y.F. Shen, Y.D. Wang, X.P. Liu, X. Sun, R. Lin Peng, S.Y. Zhang, L. Zuo, P.K. Liaw, Deformation mechanisms of a 20Mn TWIP steel investigated by in situ neutron diffraction and TEM, Acta Mater. 61 (2013) 6093–6106. https://doi.org/10.1016/j.actamat.2013.06.051.

[5] J.S. Jeong, W. Woo, K.H. Oh, S.K. Kwon, Y.M. Koo, In situ neutron diffraction

study of the microstructure and tensile deformation behavior in Al-added high manganese austenitic steels, Acta Mater. 60 (2012) 2290–2299. https://doi.org/10.1016/j.actamat.2011.12.043.

[6] L. Zhang, M. Wen, M. Imade, S. Fukuyama, K. Yokogawa, Effect of nickel equivalent on hydrogen gas embrittlement of austenitic stainless steels based on type 316 at low temperatures, Acta Mater. 56 (2008) 3414–3421. https://doi.org/10.1016/j.actamat.2008.03.022.

[7] S. Hany, M. Milochova, K. Littrell, R. Lorange, J.B. Vogt, E. Abi-Aad, E. Bychkov, Advanced characterization of cryogenic 9Ni steel using synchrotron radiation, neutron scattering and 57Fe Mössbauer spectroscopy, Mater. Des. 146 (2018) 219–227. https://doi.org/10.1016/j.matdes.2018.03.024.

[8] Y. Wang, B. Liu, K. Yan, M. Wang, S. Kabra, Y.L. Chiu, D. Dye, P.D. Lee, Y. Liu, B. Cai, Probing deformation mechanisms of a FeCoCrNi high-entropy alloy at 293 and 77 K using in situ neutron diffraction, Acta Mater. 154 (2018) 79–89. https://doi.org/10.1016/j.actamat.2018.05.013.

[9] D.G. Kim, Y.H. Jo, J. Yang, W.M. Choi, H.S. Kim, B.J. Lee, S.S. Sohn, S. Lee, Ultrastrong duplex high-entropy alloy with 2 GPa cryogenic strength enabled by an accelerated martensitic transformation, Scr. Mater. 171 (2019) 67–72. https://doi.org/10.1016/j.scriptamat.2019.06.026.

[10] J. Yoo, K. Choi, A. Zargaran, N.J. Kim, Effect of stacking faults on the ductility of Fe-18Mn-1.5Al-0.6C twinning-induced plasticity steel at low temperatures, Scr. Mater. 137 (2017) 18–21. https://doi.org/10.1016/j.scriptamat.2017.04.037.

[11] S. Huang, H. Huang, W. Li, D. Kim, S. Lu, X. Li, E. Holmström, S.K. Kwon, L. Vitos, H. Huang, D. Kim, L. Vitos, E. Holmström, S. Huang, S.K. Kwon, W. Li, H. Huang, W. Li, D. Kim, S. Lu, X. Li, E. Holmström, S.K. Kwon, L. Vitos, Twinning in metastable high-entropy alloys, Nat. Commun. 9 (2018) 2381. https://doi.org/10.1038/s41467-018-04780-x.

[12] Z. Li, K.G. Pradeep, Y. Deng, D. Raabe, C.C. Tasan, Metastable high-entropy dual-phase alloys overcome the strength–ductility trade-off, Nature. 534 (2016) 1–8. https://doi.org/10.1038/nature17981.

[13] Y. Lü, B. Hutchinson, D.A. Molodov, G. Gottstein, Effect of deformation and annealing on the formation and reversion of ε-martensite in an Fe-Mn-C alloy, Acta Mater. 58 (2010) 3079–3090. https://doi.org/10.1016/j.actamat.2010.01.045.

[14] S. Huang, W. Li, S. Lu, F. Tian, J. Shen, E. Holmström, L. Vitos, Temperature dependent stacking fault energy of FeCrCoNiMn high entropy alloy, Scr. Mater. 108 (2015) 44–47. https://doi.org/10.1016/j.scriptamat.2015.05.041.

[15] S.F. Liu, Y. Wu, H.T. Wang, J.Y. He, J.B. Liu, C.X. Chen, X.J. Liu, H. Wang, Z.P. Lu, Stacking fault energy of face-centered-cubic high entropy alloys, Intermetallics. 93 (2018) 269–273. https://doi.org/10.1016/j.intermet.2017.10.004.

[16] N.L. Okamoto, S. Fujimoto, Y. Kambara, M. Kawamura, Z.M.T. Chen, H. Matsunoshita, K. Tanaka, H. Inui, E.P. George, Size effect, critical resolved shear stress, stacking fault energy, and solid solution strengthening in the CrMnFeCoNi high-entropy alloy, Sci. Rep. 6 (2016) 1–10. https://doi.org/10.1038/srep35863.

[17] Q. Ding, X. Fu, D. Chen, H. Bei, B. Gludovatz, J. Li, Z. Zhang, E.P. George, Q. Yu, T. Zhu, R.O. Ritchie, Real-time nanoscale observation of deformation mechanisms in CrCoNi-based medium- to high-entropy alloys at cryogenic temperatures, Mater.

Today. 25 (2019) 21–27. https://doi.org/10.1016/j.mattod.2019.03.001.

[18] B. Cai, B. Liu, S. Kabra, Y. Wang, K. Yan, P.D. Lee, Y. Liu, Deformation mechanisms of Mo alloyed FeCoCrNi high entropy alloy: In situ neutron diffraction, Acta Mater. 127 (2017) 471–480. https://doi.org/10.1016/j.actamat.2017.01.034.

[19] L. Tang, K. Yan, B. Cai, Y. Wang, B. Liu, S. Kabra, M.M. Attallah, Y. Liu, Deformation mechanisms of FeCoCrNiMo0.2 high entropy alloy at 77 and 15 K, Scr. Mater. 178 (2020) 166–170. https://doi.org/10.1016/J.SCRIPTAMAT.2019.11.026.

[20] J. Liu, D. Kaoumi, Use of in-situ TEM to characterize the deformation-induced martensitic transformation in 304 stainless steel at cryogenic temperature, Mater. Charact. 136 (2018) 331–336. https://doi.org/https://doi.org/10.1016/j.matchar.2017.12.005.

[21] J.G. Kim, J.W. Bae, J.M. Park, W. Woo, S. Harjo, K.-G. Chin, S. Lee, H.S. Kim, Synergetic strengthening of layered steel sheet investigated using an in situ neutron diffraction tensile test, Sci. Rep. 9 (2019) 6829. https://doi.org/10.1038/s41598-019-43369-2.

[22] J.S. Jeong, W. Woo, K.H. Oh, S.K. Kwon, Y.M. Koo, In situ neutron diffraction study of the microstructure and tensile deformation behavior in Al-added high manganese austenitic steels, Acta Mater. 60 (2012) 2290–2299. https://doi.org/https://doi.org/10.1016/j.actamat.2011.12.043.

[23] K.S. Raghavan, A.S. Sastri, M.J. Marcinkowski, Nature of the Work-hardening Behavior in Hadfields Manganese steel, Trans Met Soc AIME. 245 (1969) 1569–1575.

[24] H. Beladi, I.B. Timokhina, Y. Estrin, J. Kim, B.C. De Cooman, S.K. Kim, Orientation dependence of twinning and strain hardening behaviour of a high manganese twinning induced plasticity steel with polycrystalline structure, Acta Mater. 59 (2011) 7787–7799. https://doi.org/10.1016/j.actamat.2011.08.031.

[25] Z.Y. Liang, Y.Z. Li, M.X. Huang, The respective hardening contributions of dislocations and twins to the flow stress of a twinning-induced plasticity steel, Scr. Mater. 112 (2016) 28–31. https://doi.org/10.1016/j.scriptamat.2015.09.003.

[26] J.R. Santisteban, M.R. Daymond, J.A. James, L. Edwards, ENGIN-X: a third-generation neutron strain scanner, J. Appl. Crystallogr. 39 (2006) 812–825. https://doi.org/10.1107/S0021889806042245.

[27] O. Kirichek, J.D. Timms, J.F. Kelleher, R.B.E.E. Down, C.D. Offer, S. Kabra, S.Y. Zhang, Sample environment for neutron scattering measurements of internal stresses in engineering materials in the temperature range of 6 K to 300 K, Rev. Sci. Instrum. 88 (2017) 25103. https://doi.org/10.1063/1.4974815.

[28] T. Ungár, A. Borbély, The effect of dislocation contrast on x-ray line broadening: A new approach to line profile analysis, Appl. Phys. Lett. 69 (1996) 3173–3175. https://doi.org/10.1063/1.117951.

[29] T. Ungár, S. Ott, P.G. Sanders, A. Borbély, J.R. Weertman, Dislocations, grain size and planar faults in nanostructured copper determined by high resolution X-ray diffraction and a new procedure of peak profile analysis, Acta Mater. 46 (1998) 3693–3699. https://doi.org/10.1016/S1359-6454(98)00001-9.

[30] R. Hielscher, C.B. Silbermann, E. Schmidl, J. Ihlemann, Denoising of crystal orientation maps, J. Appl. Crystallogr. 52 (2019) 984–996.

https://doi.org/10.1107/S1600576719009075.

[31] I.C. Jung, B.C. De Cooman, Temperature dependence of the flow stress of Fe-18Mn-0.6C-xAl twinning-induced plasticity steel, Acta Mater. 61 (2013) 6724–6735. https://doi.org/10.1016/j.actamat.2013.07.042.

[32] H. Choo, S.C. Vogel, H. Li, K. Tao, D.W. Brown, J.J. Wall, In situ neutron diffraction study of grain-orientation-dependent phase transformation in 304L stainless steel at a cryogenic temperature , J. Appl. Phys. 100 (2006) 123515. https://doi.org/10.1063/1.2402474.

[33] Y.Q. Wang, S. Hossain, S. Kabra, S.Y. Zhang, D.J. Smith, C.E. Truman, Effect of boundary conditions on the evolution of lattice strains in a polycrystalline austenitic stainless steel, J. Mater. Sci. 52 (2017) 7929–7936. https://doi.org/10.1007/s10853-017-0997-6.

[34] A. Argon, Strengthening mechanisms in crystal plasticity, Oxford University Press on Demand, 2008.

[35] R.P. Reed, R.E. Schramm, Relationship between stacking-fault energy and x-ray measurements of stacking-fault probability and microstrain, J. Appl. Phys. 45 (1974) 4705–4711. https://doi.org/10.1063/1.1663122.

[36] D. Balzar, Voigt-function model in diffraction line-broadening analysis, Microstruct. Anal. from Diffr. (1999) 44. https://doi.org/10.1.1.30.7311.

[37] V.I. Razumovskiy, C. Hahn, M. Lukas, L. Romaner, Ab initio study of elastic and mechanical properties in FeCrMn alloys, Materials (Basel). 12 (2019). https://doi.org/10.3390/ma12071129.

[38] J.A. Rayne, B.S. Chandrasekhar, Elastic constants of iron from 4.2 to 300°K, Phys. Rev. 122 (1961) 1714–1716. https://doi.org/10.1103/PhysRev.122.1714.

[39] S.M. Foiles, Temperature dependence of grain boundary free energy and elastic constants, Scr. Mater. 62 (2010) 231–234. https://doi.org/10.1016/j.scriptamat.2009.11.003.

[40] G. Laplanche, M. Schneider, F. Scholz, J. Frenzel, G. Eggeler, J. Schreuer, Processing of a single-crystalline CrCoNi medium-entropy alloy and evolution of its thermal expansion and elastic stiffness coefficients with temperature, Scr. Mater. 177 (2020) 44–48. https://doi.org/10.1016/j.scriptamat.2019.09.020.

[41] T. Teramoto, K. Yamada, R. Ito, K. Tanaka, Monocrystalline elastic constants and their temperature dependences for equi-atomic Cr-Mn-Fe-Co-Ni high-entropy alloy with the face-centered cubic structure, J. Alloys Compd. 777 (2019) 1313–1318. https://doi.org/10.1016/j.jallcom.2018.11.052.

[42] J. Kim, Y. Estrin, B.C. De Cooman, Application of a dislocation density-based constitutive model to Al-alloyed TWIP steel, Metall. Mater. Trans. A Phys. Metall. Mater. Sci. 44 (2013) 4168–4182. https://doi.org/10.1007/s11661-013-1771-2.

[43] I. Gutierrez-Urrutia, S. Zaefferer, D. Raabe, The effect of grain size and grain orientation on deformation twinning in a Fe–22wt.% Mn–0.6wt.% C TWIP steel, Mater. Sci. Eng. A. 527 (2010) 3552–3560. https://doi.org/https://doi.org/10.1016/j.msea.2010.02.041.

[44] B.C. De Cooman, O. Kwon, K.-G.G. Chin, State-of-the-knowledge on TWIP steel, Mater. Sci. Technol. 28 (2012) 513–527. https://doi.org/10.1179/1743284711Y.0000000095.

[45] D.R. Steinmetz, T. Jäpel, B. Wietbrock, P. Eisenlohr, I. Gutierrez-Urrutia, A. Saeed-

Akbari, T. Hickel, F. Roters, D. Raabe, A. Saeed–Akbari, T. Hickel, F. Roters, D. Raabe, A. Saeed-Akbari, T. Hickel, F. Roters, D. Raabe, Revealing the strain-hardening behavior of twinning-induced plasticity steels: Theory, simulations, experiments, Acta Mater. 61 (2013) 494–510. https://doi.org/10.1016/j.actamat.2012.09.064.

[46] D. Hull, D.J. Bacon, Introduction to dislocations, Elsevier, 2011.

[47] X. Gao, Y. Lu, J. Liu, J. Wang, T. Wang, Y. Zhao, Extraordinary ductility and strain hardening of Cr26Mn20Fe20Co20Ni14 TWIP high-entropy alloy by cooperative planar slipping and twinning, Materialia. 8 (2019) 100485. https://doi.org/10.1016/j.mtla.2019.100485.

[48] H. Idrissi, K. Renard, L. Ryelandt, D. Schryvers, P.J. Jacques, On the mechanism of twin formation in Fe–Mn–C TWIP steels, Acta Mater. 58 (2010) 2464–2476. https://doi.org/10.1016/J.ACTAMAT.2009.12.032.

[49] X.S. Yang, S. Sun, H.H. Ruan, S.Q. Shi, T.Y. Zhang, Shear and shuffling accomplishing polymorphic fcc γ → hcp ε → bct α martensitic phase transformation, Acta Mater. 136 (2017) 347–354. https://doi.org/10.1016/j.actamat.2017.07.016.

[50] M. Eskandari, A. Zarei-Hanzaki, M.A. Mohtadi-Bonab, Y. Onuki, R. Basu, A. Asghari, J.A. Szpunar, Grain-orientation-dependent of γ–ε–α′ transformation and twinning in a super-high-strength, high ductility austenitic Mn-steel, Mater. Sci. Eng. A. 674 (2016) 514–528. https://doi.org/10.1016/j.msea.2016.08.024.

[51] O. Bouaziz, N. Guelton, Modelling of TWIP effect on work-hardening, Mater. Sci. Eng. A. 319–321 (2001) 246–249. https://doi.org/10.1016/S0921-5093(00)02019-0.

[52] K. Jeong, J.E. Jin, Y.S. Jung, S. Kang, Y.K. Lee, The effects of Si on the mechanical twinning and strain hardening of Fe-18Mn-0.6C twinning-induced plasticity steel, Acta Mater. 61 (2013) 3399–3410. https://doi.org/10.1016/j.actamat.2013.02.031.

[53] G. Dini, R. Ueji, A. Najafizadeh, S.M. Monir-Vaghefi, Flow stress analysis of TWIP steel via the XRD measurement of dislocation density, Mater. Sci. Eng. A. 527 (2010) 2759–2763. https://doi.org/10.1016/j.msea.2010.01.033.

[54] Z. Chen, Z. Sun, B. Panicaud, Investigation of ductile damage during surface mechanical attrition treatment for TWIP steels using a dislocation density based viscoplasticity and damage models, Mech. Mater. 129 (2019) 279–289. https://doi.org/10.1016/j.mechmat.2018.12.009.

[55] H. Zhi, C. Zhang, S. Antonov, H. Yu, T. Guo, Y. Su, Investigations of dislocation-type evolution and strain hardening during mechanical twinning in Fe-22Mn-0.6C twinning-induced plasticity steel, Acta Mater. 195 (2020) 371–382. https://doi.org/10.1016/j.actamat.2020.05.062.

[56] H. Conrad, G. Schoeck, Cottrell locking and the flow stress in iron, Acta Metall. 8 (1960) 791–796. https://doi.org/https://doi.org/10.1016/0001-6160(60)90175-9.

[57] F. de las Cuevas, M. Reis, A. Ferraiuolo, G. Pratolongo, L.P. Karjalainen, J. Alkorta, J. Gil Sevillano, Hall-Petch Relationship of a TWIP Steel, Key Eng. Mater. 423 (2010) 147–152. https://doi.org/10.4028/www.scientific.net/KEM.423.147.

[58] R.J. Arsenault, Solid solution strengthening and weakening of b.c.c. solid solutions, Acta Metall. 17 (1969) 1291–1297. https://doi.org/10.1016/0001-6160(69)90144-8.

[59] S. Allain, O. Bouaziz, J.P. Chateau, Thermally activated dislocation dynamics in austenitic FeMnC steels at low homologous temperature, Scr. Mater. 62 (2010) 500–503. https://doi.org/10.1016/j.scriptamat.2009.12.026.

[60] U.F. Kocks, Realistic constitutive relations for metal plasticity, Mater. Sci. Eng. A. 317 (2001) 181–187. https://doi.org/https://doi.org/10.1016/S0921-5093(01)01174-1.

[61] N. Tsuchida, Y. Tomota, H. Moriya, O. Umezawa, K. Nagai, Application of the Kocks-Mecking model to tensile deformation of an austenitic 25Cr-19Ni steel, Acta Mater. 49 (2001) 3029–3038. https://doi.org/10.1016/S1359-6454(01)00197-5.

[62] Y.P. Varshni, Temperature dependence of the elastic constants, Phys. Rev. B. 2 (1970) 3952–3958. https://doi.org/10.1103/PhysRevB.2.3952.

[63] P.S. Follansbee, U.F. Kocks, A constitutive description of the deformation of copper based on the use of the mechanical threshold stress as an internal state variable, Acta Metall. 36 (1988) 81–93. https://doi.org/https://doi.org/10.1016/0001-6160(88)90030-2.

[64] R.S. Ganji, P. Sai Karthik, K. Bhanu Sankara Rao, K. V. Rajulapati, Strengthening mechanisms in equiatomic ultrafine grained AlCoCrCuFeNi high-entropy alloy studied by micro- and nanoindentation methods, Acta Mater. 125 (2017) 58–68. https://doi.org/10.1016/j.actamat.2016.11.046.

[65] I. Gutierrez-Urrutia, S. Zaefferer, D. Raabe, The effect of grain size and grain orientation on deformation twinning in a Fe-22wt.% Mn-0.6wt.% C TWIP steel, Mater. Sci. Eng. A. 527 (2010) 3552–3560. https://doi.org/10.1016/j.msea.2010.02.041.

[66] I. Gutierrez-Urrutia, D. Raabe, Dislocation and twin substructure evolution during strain hardening of an Fe-22 wt.% Mn-0.6 wt.% C TWIP steel observed by electron channeling contrast imaging, Acta Mater. 59 (2011) 6449–6462. https://doi.org/10.1016/j.actamat.2011.07.009.

[67] I. Gutierrez-Urrutia, D. Raabe, Study of Deformation Twinning and Planar Slip in a TWIP Steel by Electron Channeling Contrast Imaging in a SEM, Mater. Sci. Forum. 702–703 (2011) 523–529. https://doi.org/10.4028/www.scientific.net/msf.702-703.523.

[68] J. Gil Sevillano, F. De Las Cuevas, Internal stresses and the mechanism of work hardening in twinning-induced plasticity steels, Scr. Mater. 66 (2012) 978–981. https://doi.org/10.1016/j.scriptamat.2012.02.019.

[69] J. Gil Sevillano, An alternative model for the strain hardening of FCC alloys that twin, validated for twinning-induced plasticity steel, Scr. Mater. 60 (2009) 336–339. https://doi.org/10.1016/j.scriptamat.2008.10.035.

[70] P. Kusakin, A. Belyakov, C. Haase, R. Kaibyshev, D.A. Molodov, Microstructure evolution and strengthening mechanisms of Fe-23Mn-0.3C-1.5Al TWIP steel during cold rolling, Mater. Sci. Eng. A. 617 (2014) 52–60. https://doi.org/10.1016/j.msea.2014.08.051.

[71] I. Shakhova, V. Dudko, A. Belyakov, K. Tsuzaki, R. Kaibyshev, Effect of large strain cold rolling and subsequent annealing on microstructure and mechanical properties of an austenitic stainless steel, Mater. Sci. Eng. A. 545 (2012) 176–186. https://doi.org/10.1016/j.msea.2012.02.101.

[72] R.L. Fullman, Measurement of Particle Sizes in Opaque Bodies, JOM. 5 (1953) 447–452. https://doi.org/10.1007/bf03398971.

[73] P. Zhou, Z.Y. Liang, R.D. Liu, M.X. Huang, Evolution of dislocations and twins in a strong and ductile nanotwinned steel, Acta Mater. 111 (2016) 96–107.

https://doi.org/10.1016/j.actamat.2016.03.057.

[74] Z.C. Luo, M.X. Huang, Revisit the role of deformation twins on the work-hardening behaviour of twinning-induced plasticity steels, Scr. Mater. 142 (2018) 28–31. https://doi.org/10.1016/j.scriptamat.2017.08.017.

[75] Z.-H. Jin, P. Gumbsch, E. Ma, K. Albe, K. Lu, H. Hahn, H. Gleiter, The interaction mechanism of screw dislocations with coherent twin boundaries in different face-centred cubic metals, Scr. Mater. 54 (2006) 1163–1168. https://doi.org/https://doi.org/10.1016/j.scriptamat.2005.11.072.

[76] T.S. Byun, N. Hashimoto, K. Farrell, Temperature dependence of strain hardening and plastic instability behaviors in austenitic stainless steels, Acta Mater. 52 (2004) 3889–3899. https://doi.org/https://doi.org/10.1016/j.actamat.2004.05.003.

[77] J. Chen, J.J. Wang, G. Yuan, C.M. Liu, Twin boundary bending during tensile deformation and its temperature dependence, Mater. Sci. Eng. A. 759 (2019) 47–54. https://doi.org/10.1016/j.msea.2019.04.097.

[78] Y.G. Kim, J.M. Han, J.S. Lee, Composition and temperature dependence of tensile properties of austenitic Fe-Mn-Al-C alloys, Mater. Sci. Eng. A. 114 (1989) 51–59. https://doi.org/10.1016/0921-5093(89)90844-7.

List of Tables

Table 1. Mechanical properties of the alloy deformed at different temperatures;

Table 2. Various properties of the TWIP steel at different temperature;

Table 3. σ_{diff} at two strain levels using different α values;

List of Figures

Fig. 1 (a) Schematic illustration of in situ neutron diffraction facility at ISIS; (b) the cryogenic chamber and hydraulic system; and (c) the size of tensile bar.

Fig. 2 The microstructure of the as-fabricated TWIP alloy: (a) typical IPF map, perpendicular to rolling direction (RD); (b) grain misorientation distribution (The black line shows the random distribution misorientation); (c) HAADF-STEM image of a dislocation tangling zone and (d) typical bright field image and selected area diffraction pattern of a dislocation-free zone.

Fig. 3 Mechanical performance of the TWIP steel at different temperatures: (a) true stress-strain curves; (b) mechanical properties versus temperatures; and (c) strain hardening rate.

Fig. 4 Diffraction patterns with respect to true stress when deforming at (a) 373 K and (b) 77 K; Normalized intensity as a function of true strain at (c) 373 K and (d) 77 K.

Fig. 5 Lattice strain curves of crystallographic planes {111}, {200}, {220}, {311} and {222} obtained from the axial and radial detectors during deforming at different temperatures: (a) 373 K (b) 293 K (c) 173 K and (d) 77 K.

Fig. 6 Evolution of lattice strain and stacking fault probability as a function of true strain at different temperature: (a) 373 K, (b) 293 K, (c) 173 K and (d) 77 K.

Fig. 7 (a) Temperature dependence of stacking fault probability and stacking fault energy and (b) dislocation density evolution with true strain at different temperatures.

Fig. 8 Grain morphology observed by OM in TWIP steel deformed at 293 K and 77 K with different true strain: (a) 293 K, ε=~0.1; (b) 293 K, ε=~0.2; (c) 293 K, ε=~0.3; (d) 77 K, ε=~0.1; (e) 77 K, ε=~0.2; (f) 77 K, ε=~0.3.

Fig. 9 EBSD image quality maps showing the twinning gathering process with increasing tensile strain at 77 K: (a) strain of 0.05; (b) higher magnification of the rectangle zone in (a); (c) strain of ~0.1; (d) strain of ~0.2.

Fig. 10 TEM images taken from the sample deformed to true strain ~0.3 at 373 K and 77 K. (a and c) bright filed image at 373 K and 77 K, respectively; (b and d) SAED patterns of (a and c), respectively; shows that the twin density increases with the deformation temperature decreasing and FCC-γ to HCP-ε transition occurred at 77 K.

Fig. 11 Twinning formation and γ→ε phase transformation of the alloy during deformed at 77 K to a true strain of ~0.3: (a) HRTEM image; (b) atomic image of A area in (a); (c) higher magnification of the white rectangle areas in (b) and (d-g) FFT images at areas of A, B, C and D in (a).

Fig .12 (a) Temperature dependence of the shear modulus and lattice parameter of the alloy and (b) normalized thermally activated component of the yielding stress with respect to the normalized temperature.

Fig. 13 (a) The respective contribution of multiple resources to the total flow stress; strain hardening contribution from (b) dislocation and (c) twin density at different temperatures; (d) temperature dependence of the hardening rate from dislocation and twinning.